Table 1 – Distribution of GlcAT transcripts in adult mouse brain

	GlcAT-P	GlcAT-S
Olfactory system		
Olfactory bulb		
Glomerular layer	++	++
Mitral cell layer	++	0
Anterior olfactory nu.	+++	0
Basal forebrain		
Caudate putamen/globus pallidus	+/++[a]	0
Ventral pallidum	++[a]	+
Stria terminalis	+	+
Substantia nigra pars compacta	+++[a]	0
Lateral septum	+++	++
Medial septum/diagonal band	++	+
Amygdaloid complex		
Central/medial amygdaloid nu.	++	+
Amygdalohippocampal area	+	++
Hippocampal formation		
Hippocampus		
CA1 subfield	+++	±
CA2/CA3 subfield	+++	+++
Dentate granule cell layer	+++	0
Dentate polymorphic layer	++++[a]	0
S. oriens/lucidum/radiatum	++[b]	++[b]
S. lacunosum-moleculare	0	0
Subiculum	+	++
Cerebral cortex		
Isocortex layers		
I	0	0
II	+++	0
III	±	0
IV	++	++[d]
V	+++	+++[a]
VI	+++	+++[a]
Orbital cortex	++	++[a]
Piriform cortex	+++	+
Indusium griseum	±	++
Ectorhinal cortex	+++	+++
Endopiriform cortex	+[c]/++	+++
Claustrum	++	+++
Cingulate/retrosplenial cortices	++	++[b]
Thalamus		
Ventroposterior/posterior nu.	+	+
Lateral/medial geniculate nu.	+	++/+++
Ventrolateral/ventromedial	++	0
Anteroventral/anterodorsal thalamic nu.	++/++	++/+++
Anteromedial/mediodorsal nu.	++	++
Paraventricular/centromedial nu.	+++/+	+++/++
Paracentral/centrolateral nu.	+	+
Rhomboid/reuniens nu.	++	+
Parafascicular nu.	+	++
Reticular nu.	+	±
Medial/lateral habenular nu.	++++/+++[a]	0/++
Hypothalamus		
Dorsomedia hypothalamic nu.	+	++
Ventromedial hypothalamic nu.	+++	++
Arcuate hypothalamic nu.	0	+++
Lateral hypothalamic nu.	+	+
Supraammillary nu.	++	++
Hypothalamus		
Medial/lateral mammilary nu.	+	0
Pretectal nu. group	+	+
Midbrain and pons		
Superior/inferior colliculus	++/+++	+/++[a]
Periaquidauctal gray	+	+
Interpeduncular nu.	+++	++[a]
Red nu.	±	++[a]
Lateral lemuniscus	+++	++
Pontine/reticulotegmental nu.	++	±/++
Pontine reticular field	+	±
Dorsal tegmental nu.	+++	++
Parabrachial nu.	+++	++
Parabigeminal nu.	++++	++
Dorsal/median raphe nu.	++	+
Superior olive	++	0
Medulla		
Giantcellular reticular nu.	++[a]	±
Raphe magnus/pallidus/obscurus nu.	+	+
Inferior olive/lateral reticular nu.	0	0
Cuneate nu.	++	+
Cranial nerve nuclei		
Oculomotor (3)	+++	++
Trigeminal nu. (5)		
Motor trigeminal nu.	+	±
Ventrolateral trigeminal nu.	+++	++
Spino-trigeminal nu.	+++	+
Principal sensory trigeminal nu.	+++	+
Mesencephalic trigeminal nu.	+++[b]	0
Vestibular nu. group(8)	++	++
Cochlear nu. group	+++	++
Prepositus hypoglossal nu.	+	++
Cerebellum		
Molecular cell layer	+	±
Purkinje cell layer	+++	±
Granular cell layer	0	+
Deep cerebellar nu.	+++	±
Others		
Choroid plexus	0	0
Ependyma and pia mater	0	0
Subfornical organ	0	++

nu., nucleus; ++++, very high; +++, high; ++, moderate; +, low; ±, very low; 0, less than threshold.
[a]A few cells positive for mRNA.
[b]Few cells positive for mRNA.
[c]In the anterior part.
[d]In the parietal cortex, there were few cells positive for mRNA.
In GlcAT-P-deficient mouse brains, there were no signals using GlcAT-P cRNA. There were no differences in the distributions of GlcAT-S mRNA in brains between wild-type and GlcAT-P-deficient mice.

containing cells expressed with GlcAT-S mRNA between wild-type and GlcAT-P-deficient mice (data not shown).

Next we performed immunohistochemistry to investigate the distribution of HNK-1 carbohydrate epitope, which is synthesized by GlcAT enzymes (Fig. 2 and Table 2) and

compared the regions expressing the GlcAT enzymes with the areas containing HNK-1 carbohydrate in the adult mouse brain with or without the GlcAT-P gene. First, in the wild-type mice, the HNK-1 carbohydrate was widely distributed over most of the mouse brain, which reflected the expression patterns of the GlcAT-P mRNAs. Especially, among regions containing a high level of GlcAT-P mRNA, the lateral septum (LS; Figs. 2B-a and j), the hippocampal complex (Hip; Figs. 2A-c and h), and the interpeduncular nucleus (IP; Figs. 2A-d and i) in the limbic system and the cochlear nucleus (VC; Figs. 2A-e and j) and the lateral lemuniscus (LL; Figs. 2B-b, h, k, and q), the inferior colliculus (IC; Figs. 2A-e and j), the parabigeminal nucleus (PBG; Figs. 2B-b, e, k, and n), the parabrachial nuclei (PB; Figs. 2A-e and j), and the trigeminal sensory system (Pr5; Figs. 2A-e and j), and the dorsal column nuclei (Cu; Figs. 2B-d and m) in the sensory system showed very intense staining of the HNK-1 antibody. On the other hand, among areas containing little GlcAT-P or GlcAT-S mRNAs, the medial nuclei of the bed nucleus of the stria terminalis (BST; Figs. 2A-b and g), the reticular nucleus of the thalamus (Rt; Figs. 2A-c and h), and the precerebellar nuclei containing the inferior olive (IO; Figs. 2B-f and o), and the lateral reticular nucleus (LRt; Figs. 2B-i, o, and r), expressed the HNK-1 carbohydrate diffusely. These nuclei also expressed the HNK-1 carbohydrate strongly in GlcAT-P-deficient mouse brain. In addition, the SFO, the Arc, and the MG, which showed very intense signals of GlcAT-S mRNA, contained little HNK-1 carbohydrate in mice with or without GlcAT gene.

In the present study, we also compared the HNK-1 carbohydrate expression in the layer of the cortex and the cerebellum between wild-type and GlcAT-P-deficient mice (Fig. 3). In the cortex, wild-type mice expressed GlcAT-P in layer II to VI (Fig. 3A), which was likely to have led to the expression of HNK-1 carbohydrate in most layers, including very intense signals in the layer II (Fig. 3B). On the other hand, GlcAT-P-deficient mice expressed a little GlcAT-S and HNK-1 carbohydrate in layers V–VI of most of the isocortex (Figs. 1B and 2A-g, h, and i), while in the parietal cortices (Waite, 2004), the presence of GlcAT-S was observed in layers V–VI (Fig. 3C) and the presence of HNK-1 carbohydrate in layers III to VI (Fig. 3D). In the cerebellum of wild-type, the purkinje cells expressed GlcAT-P (P; Fig. 3E) and the molecular layer strongly contained high levels of HNK-1 carbohydrate (M; Fig. 3F). In addition, HNK-1 signals were also seen as several neuronal spots in the granular cell layers of the wild-type and GlcAT-P-deficient mice (arrowhead in G; Fig. 3F) and the dotted signals still left in the granular layer of GlcAT-P-deficient mice (arrowheads in G; Fig. 3H), which seemed to be due to the presence of GlcAT-S transcripts (white arrowhead in G; Fig. 3G).

2.2. *Regulated expression of GlcAT-S in the hippocampus in mice with GlcAT-P deficiency*

We have previously reported that GlcAT-P-deficient mice exhibited reduced long-term potentiation (LTP) at the Schaffer collateral-CA1 synapses (Yamamoto et al., 2002). One matter for concern is whether GlcAT-S compensated for the lack of GlcAT-P enzyme activity for production of HNK-1 in the hippocampus of the GlcAT-P-deficient mice. In the present study, we found that the level of GlcAT-S transcripts in the CA3-subfield of GlcAT-P-deficient mice was higher than that in wild-type, especially an increase of 1.7-fold was observed in the CA3a containing the Schaffer collateral fibers projecting to the CA1-subfield (Figs. 4C, D, and J). The HNK-1 carbohydrate was expressed strongly in the polymorphic layer (Figs. 2A-h and 5H) and the CA3a (Fig. 5E). However, in the strata oriens and radiatum and the pyramidal cell layer of the CA1-subfield, HNK-1 signals were localized mostly in neuronal cells containing parvalbumin signals (Figs. 5A, D, and G), a marker for the interneuron (Kosaka et al., 1987). On the other hand, there were little differences of immunoreactions of HNK-1 or WFA between wild-type and GlcAT-P-deficient mice (Fig. 6).

3. Discussion

HNK-1 carbohydrate epitope is a sulfated trisaccharide, $HSO_3$3GlcAβ1-3Galβ1-4GlcNAc (Chou et al., 1986; Voshol et al., 1996), and key enzymes in the biosynthesis of the epitope are two different glucuronyltransferases (GlcAT-P and GlcAT-S) (Seiki et al., 1999; Shimoda et al., 1999; Terayama et al., 1997, 1998). Although these enzymes have different acceptor specificities in vitro assay system (Kakuda et al., 2005), the critical acceptor specificity is dependent on in which cells the enzyme meets with acceptor substrates. In the brain, with its great variations in the cell populations and their connections, it is important to provide information about the expression of these enzymes in the particular cells and fibers. In the present study, we determined directly brain regions containing cells expressing two enzymes by detecting their transcripts not showing displacements and projections. The major findings of the present study were the regional specificities of GlcAT transcripts and HNK-1 carbohydrate epitope.

HNK-1 carbohydrate epitope was distributed widely in the adult mouse brain and there were two patterns of HNK-1 immunostaining: spotted and diffuse signals (Table 2, S and D). Diffuse signals are likely to be brought through efferents from the regions expressing GlcAT transcripts. The epitope was especially concentrated as strong signals in the limbic-related, the sensory, and the cerebellar systems. The present findings suggested that HNK-1 carbohydrate networks tended to be especially concentrated in the septal regions among the limbic-related systems (Risold, 2004). First, GlcAT transcripts and HNK-1 carbohydrate were localized strongly in the lateral septal region (LS), the hippocampus, and the paraventricular thalamic nucleus (PV). These regions are connected as follows: (1) the LS receives ipsilateral afferents from the CA1-subfield and bilateral ones from the CA3-subfield of the hippocampus, (2) axons from the LS innervate the midline nuclei of the thalamus, especially the PV, and (3) afferents from the PV project to the hippocampal formation. Next, the present study also showed that the bed nucleus of the stria terminallis (BST) expressed the HNK-1 carbohydrate very strongly and diffusely, but not GlcAT transcripts. The expression of HNK-1 carbohydrate is reasonable because the stria terminalis is one of four main routes of afferents and efferents of the septal region; the stria terminalis, the fornix,

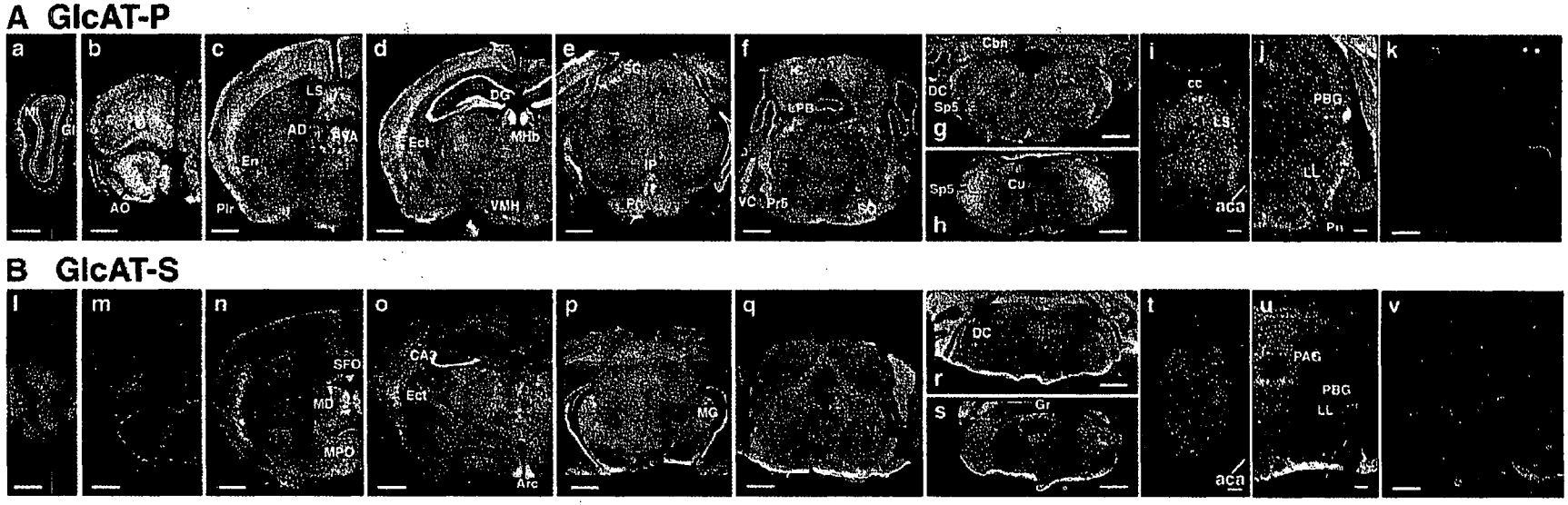

Fig. 1 – Micro-autoradiogram showing GlcAT-P (A) and GlcAT-S (B) cRNA labeling patterns in coronal sections (14 μm thick) of mouse brain. Dark-field images of emulsion-dipped coronal sections in the olfactory structure (a, l); in coronal planes at the level of the olfactory nu. (b, m); at the anterior thalamic nu. (c, n); at the habenular nu. (d, o); at the interpeduncular nu. (e, p); at the inferior colliculus (f, q); at the vestibular nu. (g, r); at the spinal trigeminal nu. (h, s); at the lateral septal nu. (i, t); at the lateral lemuniscus (j, u); at the habenular nu. with sense probe (k, v). Stars indicate artifacts (b, d–f, and o). Scale bar=1 mm in a–h, k, l–s, and v; 400 μm in i, j, t, and u.

the medial forebrain bundle, and the stria medullaris. In addition, the LS connects extensively with the medial zone of the hypothalamus and then the medial zone connects with the medial nuclei of the BST. As the ventromedial hypothalamic nucleus (VMH) in the medial zone of the hypothalamus (Simerly, 2004) expressed both GlcAT mRNAs

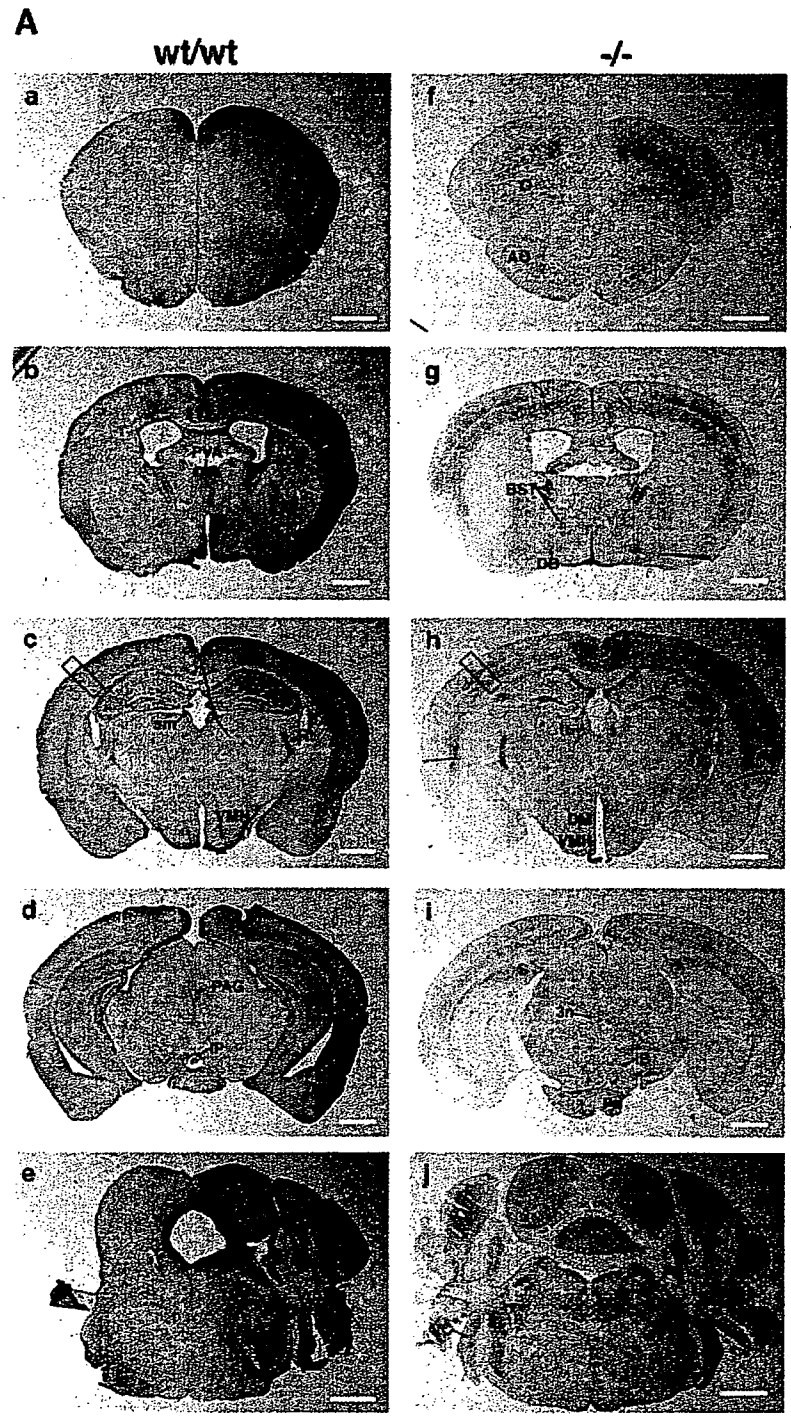

Fig. 2 – Comparison of HNK-1 carbohydrate expressions in the coronal section of GlcAT-P-deficient mice and normal littermates. Representative immunohistochemical micrograph with anti-HNK-1 antibody. Brightfield images of coronal sections (14 μm thick) of mouse brain with (w/w; A-a–e and B-a–i) or without (–/–; A-f–j and B-j–r) GlcAT-P gene. Regions in the rectangles in A-c and A-h are expanded in Figs. 3B and D. Regions in the rectangles in a and j are magnified in the insets (B). Differential interference contrast images (insets of a and j, e, g–i, n, and p–r) (B). Scale bar=1 mm in A; 200 μm as black bars in B; 50 μm as white bars in B.

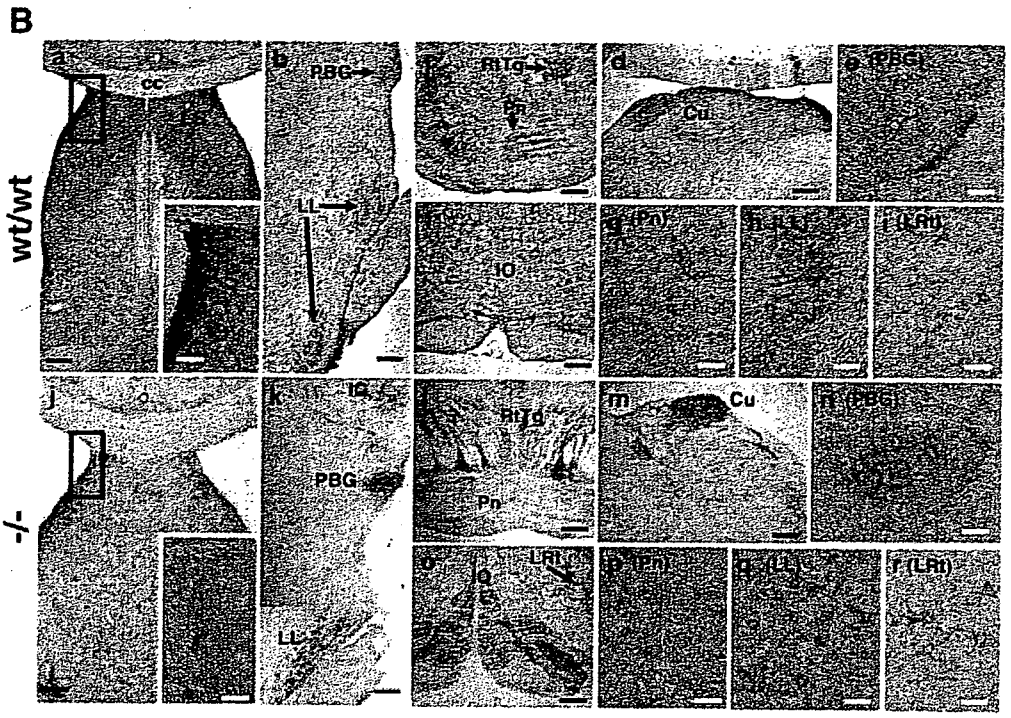

Fig. 2 (*continued*)

strongly, the HNK-1 carbohydrate seems to be present at high levels in the BST of both wild-type and GlcAT-P-deficient mice. The LS is also directly connected with the periventricular zone of the hypothalamus. The arcuate hypothalamic nucleus (Arc) in the periventricular zone (Simerly, 2004) expressed GlcAT-S mRNA strongly, which might be involved in any controls of neuroendocrine and autonomic responses. Finally, there was a system in which the stria medullaris (sm; Fig. 2A-c) and the fasciculus retroflexus (fr; Fig. 2A-h) projected from the septal regions. In this network, the septal afferents project through the stria medullaris to the medial habenular nucleus (MHb) and the projections continue in the fasciculus retroflexus to reach the IP. In this network, very intense expressions of GlcAT-P in the MHb and the IP (Figs. 1A-d and e) seemed to induce very strong expression of HNK-1 carbohydrate in the stria medullaris (sm; Fig. 2A-c) and the IP (Fig. 2A-d). On the other hand, the other neurons in the basal forebrain except for the septum connect with the lateral habenular nucleus (LHb) through the stria medullaris. Therefore, moderate expression of GlcAT-S in the LHb might induce moderate expression of HNK-1 carbohydrate in the fasciculus retroflexus (fr; Fig. 2A-h) and the IP (Fig. 2A-i), as suggested by the results of immunohistochemistry in GlcAT-P-deficient mouse brain. The present study showed that two nuclei showing expression of GlcAT-P mRNA at the ++++ level (Table 1) were the MHb and the parabigeminal nucleus (PBG). It is reported that these nuclei contain a dense aggregate of cholinergic neurons, while the sept-hippocampal cholinergic pathway contains basal forebrain cholinergic neurons (Butcher, 1995, 2004). It is possible that at least a part of the subpopulations composed of neurons expressing GlcAT-P and then catalyzing the HNK-1 carbohydrate synthesis belong to the cholinergic system.

Kosaka et al. have previously showed that a part of neurons with HNK-1 immunostaining contained Ca^{2+}-binding protein parvalbumin (Kosaka et al., 1990, 1992). On the other hand, the present study showed that most neurons with HNK-1 immunostaining were a subpopulation of interneurons immunopositive for parvalbumin in the hippocampus and the cerebral cortices (Fig. 5J) of GlcAT-P-deficient mice. The strong staining of HNK-1 in the hippocampus was induced by the expression of GlcAT-S mRNA in the CA3a. It has been previously reported that LTP was increased by application of anti-HNK-1 antibody into the stratum radiatum (Saghatelyan et al., 2000). The findings of the present study suggest that the antibody was targeted to interneurons expressing the HNK-1 carbohydrate that GlcAT-S synthesized, resulting in the reduction of the efficacy of evoked GABA release. Alternatively, as GlcAT-P was expressed in pyramidal neurons of the CA1–3 subfields, the present study also confirmed a previous report showing that the HNK-1 carbohydrate synthesized by GlcAT-P activity directly affects the increase of LTP at the Schaffer collateral-CA1 synapses (Yamamoto et al., 2002).

Among the sensory systems (Malmierca and Merchán, 2004), the auditory system was most markedly enriched in GlcAT transcripts. For example, the cochlear nuclear complex provides the first relay center in the ascending pathway of the auditory process and the axons project into the lateral lemniscus (LL); especially, afferent projections to the ventral complex of the LL arise mainly from the contralateral side of

Table 2 – Distribution of HNK-1 in GlcAT-P-deficient mice

Olfactory system	+/+	−/−
Olfactory bulb	D	N
Granular cell layer		
Mitral cell layer	D	N
Anterior olfactory nu.	DS	S
Basal forebrain		
Caudate putamen/globus pallidus	D^W	N/D
Ventral pallidum	D	D
Stria terminalis	D^S	D^S
Substantia nigra pars compacta	N	N
Lateral septum	D^S	S^a
Medial septum/diagonal band	D^W	S^a/DS^a
Amygdaloid complex		
Central/medial amygdaloid nu.	D	N
Amygdalohippocampal area	D	N
Hippocampal formation		
Hippocampus[b]		
CA1 subfield	D	S
CA2/CA3 subfield	D	S
Dentate granule cell layer	D	S^a
Dentate polymorphic layer		
S. oriens/lucidum/radiatum	D^S	S
S. lacunosum-moleculare	N	N
Subiculum	DS	S
Cerebral cortex		
Isocortex layers		
I	N	N
II	D	N
III	D	S^{ac}
IV	N	S^c
V	DS	S
VI	DS	S
Orbital cortex	D	S
Piriform cortex	D^W	N
Indusium griseum	D	S^a
Ectorhinal cortex	D	D
Endopiriform cortex	D	D
Claustrum	D	D
Cingulate/retrosplenial cortices	DS	D^S
Thalamus		
Ventroprosterior/Posterior nu.	D^W	D^W/N
Lateral/medial geniculate nu.	D^W	N
Ventrolateral/ventromedial	D^W	N
Anteroventral/anterodorsal thalamic nu.	D^W	D^W
Anteromedial/Mediodorsal nu.	D^W	D^W
Paraventricular/ centromedial nu. nu.	D^S/D^W	D^W
Paracentral/centrolateral nu.	D^W	D^W
Rhomboid/reuniens nu.	D^W	D^W
Parafascicular nu.	D^W	N
Reticular nu.	D^S	D^S
Medial/lateral habenular nu.	D/D^W	N/D
Hypothalamus		
Dorsomedial hypothalamic nu.	D	D^S
Ventromedial hypothalamic nu.	D^S	D^S
Arcuate hypothalamic nu.	D^W	D^W
Lateral hypothalamic nu.	D^W	N
Supramammillary nu.	D	D^W
Medial/lateral mammilary nu.	D	D
Pretectal nu. group	D^W	S

Table 2 (*continued*)

Olfactory system	+/+	−/−
Midbrain and pons		
Superior/inferior colliculus	D^W/D^SS^S	S/S^S
Periaquiductal gray	D^S	D
Interpeduncular nu.	D^S	D
Red nu.	S^a	DS
Lateral lemuniscus	S^S	S^S
Pontine/reticulotegmental nu.	S/S^S	D/D^S
Pontine reticular field	D^W	D^W
Dorsal tegmental nu.	DS	DS
Parabrachial nu.	D^SS^S	S^S
Parabigeminal nu.	D^SS^S	D^SS^S
Dorsal/median raphe nu.	D	D/S
Superior olive	DS	0
Medulla		
Giantcellular reticular nu.	D	D^w
Raphe magnus/pallidus/obscurus nu.	D	D^W
Inferior olive	D	DS^{Sd}
Lateral reticular nu.	D	D^S
Cuneate nu.	D^S	D^S
Cranial nerve nuclei		
Oculomotor (3)	N	S^S
Trigeminal nu.	D^W	N
Motor trigeminal nu.	DS	S^S
Ventrolateral trigeminal nu.	DS	S^S
Spino-trigeminal nu.	D^SS^S	S^S
Principal sensory trigeminal nu.	D^SS^S	S^S
Mesencephalic trigeminal nu.	N	N
Vestibular nu. group (8)	D	S^S
Cochlear nu. group	DS^S	S^S
Prepositus hypoglossal nu.	D	D
Cerebellum		
Molecular cell layer	D	N
Purkinje cell layer	S	N
Granular cell layer	S^a	D^WS^a
Deep cerebellar nu.	DS^S	DS^S
Others		
Choroid plexus	N	N
Ependyma and pia mater	N	N
Subfornical organ	N	N

nu., nucleus; D, diffuse signals positive for HNK-1; S, spotted signals in cells positive for HNK-1; N, negative.
[a] A few cells were positive for HNK-1.
[b] There were no signals in the hippocampal pyramidal cells of either type of mouse brain.
[c] The spotted signals in layer III and IV were observed only in the parietal cortex.
[d] There was an especially strong signal in the beta subnucleus of the inferior olive.
[W] Weak signals.
[S] Strong signals.

the ventral cochlear nucleus (VC). Then the LL and cochlear nuclei project axons to the inferior colliculus (IC) directly. GlcAT transcripts and HNK-1 carbohydrate were concentrated in these three nuclei. On the other hand, the medial geniculate of the thalamus (MG) contained only GlcAT-S mRNA, but little GlcAT-P mRNA or HNK-1 carbohydrate. The MG, which is the last center for auditory processing before inputs reach the

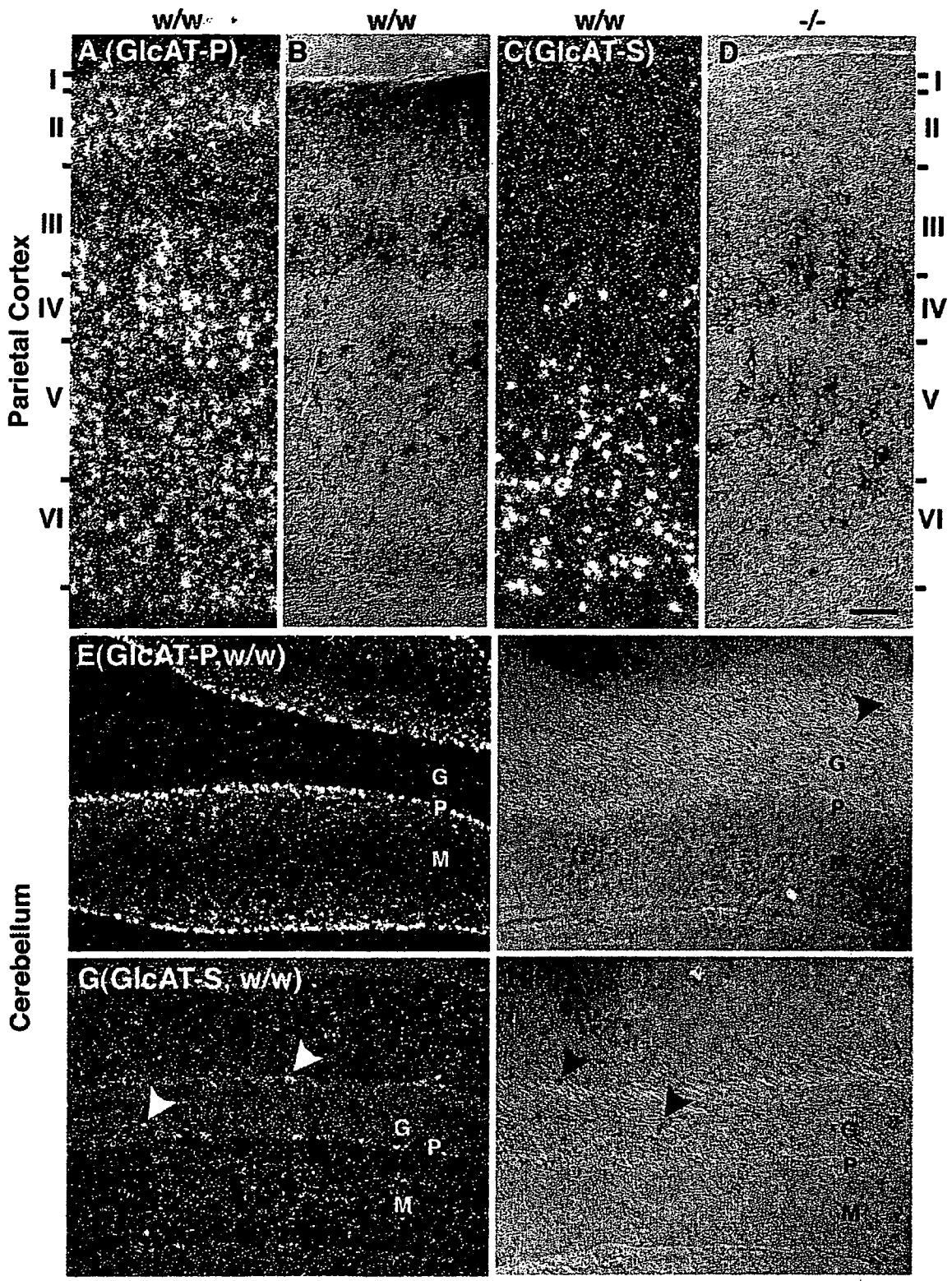

Fig. 3 – Expression of GlcAT transcripts and HNK-1 carbohydrate in the parietal cortex (A–D) and the cerebellum (E–H) of mouse brain. Dark-field images of *in situ* hybridization (A, C, E, and G), differential interference contrast images of immunohistochemistry (B, D, F, and H). I–VI, layers of the cerebral cortex; G, granular cell layer; M, molecular layer; P, Purkinje cell layer of the cerebellum. GlcAT-P (A and E); GlcAT-S (C and G); HNK-1 (B, D, F, and H). Wild-type (A–D, E, F, and G); –/– (D and H). Cellular patterns of GlcAT-S transcript in C and G were the same as those in –/– mice. Scale bar = 100 μm.

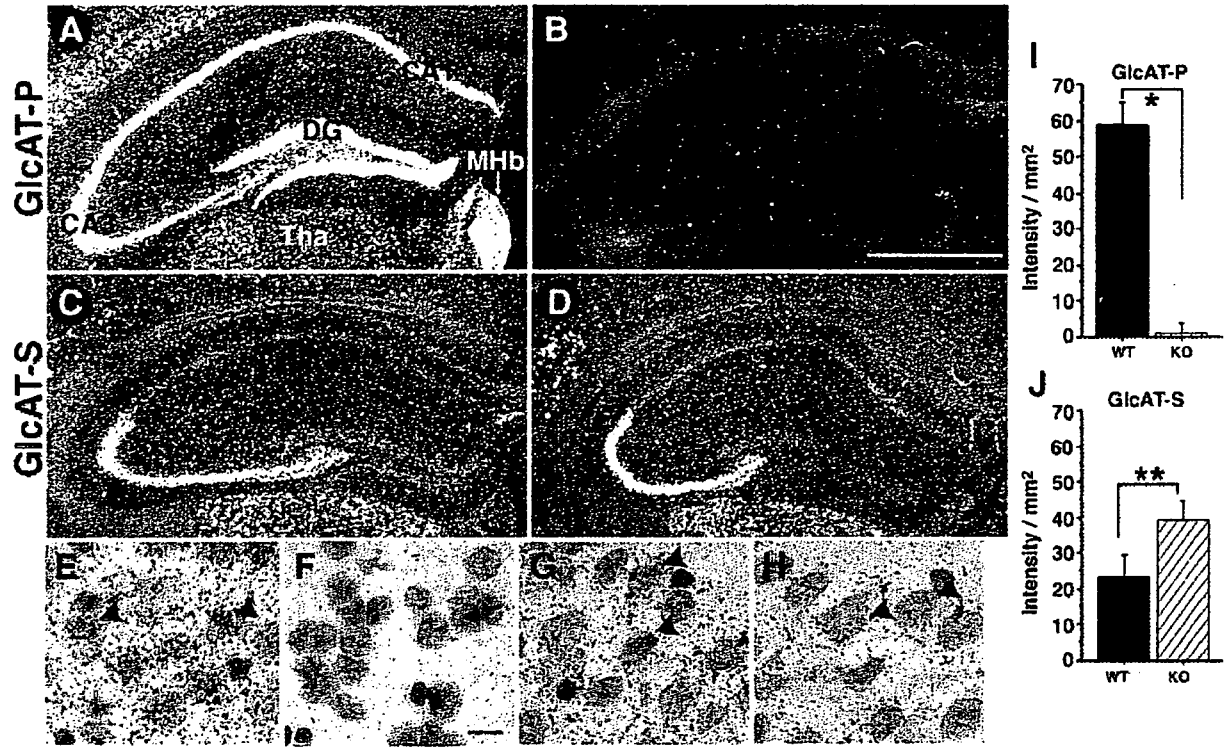

Fig. 4 – Comparisons of GlcAT transcripts in the hippocampus between wild-type (wt/wt; A, C, E, and G) and GlcAT-P-deficient (–/–; B, D, F, and H) mice. Microautoradiography of *in situ* hybridization in the hippocampus under dark-field illumination (A–D) and bright-field illumination (E–H). Scale bars = 1 mm (A–D) and 10 μm (E–H). GlcAT-P cRNA (A, B, E, and F) and GlcAT-S cRNA (C, D, G, and H). Arrowheads show neuronal cells containing signals. Comparisons of GlcAT-P and GlcAT-S transcripts between wild-type and GlcAT-P-deficient mice (I and J). ■ WT, □ GlcAT-P column and vertical line, mean (+SD) signal intensity per mm². Statistical significance of the differences was determined by paired *t*-test (*$p<0.0001$ for GlcAT-P; **$p=0.0014$ for GlcAT-S). The data show the lack of signal of GlcAT-P cRNA in the hippocampus of GlcAT-P-deficient mice (B, F, and I).

auditory cortex, receives axons from the IC and part of the efferents from the MG project to the reticular nucleus of the thalamus (Rt) containing all GABAergic and parvalbumin-positive neurons. As the Rt showed very strong labeling of HNK-1, several efferents from the MG might contribute to the very strong labeling of HNK-1 in the Rt (Groenewegen and Witter, 2004). On the other hand, the strong labeling in the Rt might also be dependent on projections from layer VI of the cerebral cortex, because afferents to the Rt mainly originate in layer VI. However, like the MG, the Arc and the subfornical organ (SFO) also showed strong positivity of GlcAT-S mRNA but not GlcAT-P mRNA nor HNK-1 carbohydrate. The possibility still exists that GlcAT-S enzyme exerts activity toward another acceptor substrate other than HNK-1 in those nuclei. Concerning the somatosensory system (Tracey, 2004), the cuneate nucleus (Cu) and the gracile nucleus (Gr) expressed GlcAT mRNAs moderately and the HNK-1 carbohydrate very intensely. These nuclei belong to the dorsal column nuclei, which receive somatosensory afferents originated in cell bodies in the dorsal root ganglia. As the dorsal column nuclei also receive afferent fibers from the trigeminal nerve, the trigeminal nuclei expressing GlcAT mRNAs and the HNK-1 carbohydrate at high levels might provide the carbohydrate to the Cu and the Gr. These nuclei connect with the ventroposterial thalamic nuclei and the fibers continue to layer IV of the parietal cortex (Waite, 2004). The pathway might, especially, contribute to the strong labeling of HNK-1 in layer IV of GlcAT-P-deficient mice (IV; Fig. 3D).

Concerning the cerebellar system, the precerebellar nuclei (Ruigrok, 2004) showed very strong HNK-1 staining in both wild-type and GlcAT-P-deficient mice. While the pontine nuclei (Pn; Figs. 2B-c, g, l, and p) including the reticulotegmental nucleus (RtTg; Figs. 2B-c and l) expressed moderate signals of the GlcAT transcripts (Figs. 1j and u), the IO and the LRt expressed weak ones (Figs. 1h and s). As afferents to the Pn generally arise from layer V neurons of the ipsilateral cortices, where GlcAT mRNAs and the HNK-1 carbohydrate are expressed, the HNK-1 carbohydrate might be supplied more from layer V to the Pn. The fact that afferent pathways to the IO mainly arise from somatosensory nuclei, such as the spinal trigeminal nucleus and the dorsal column nuclei, where HNK-1 was expressed very strongly, is in accord with the finding that the IO showed diffuse HNK-1 staining. Efferent fibers of the IO are the sole source of cerebellar climbing fibers and terminate on the dendritic tree of Purkinje cells in the molecular layer, in which Purkinje

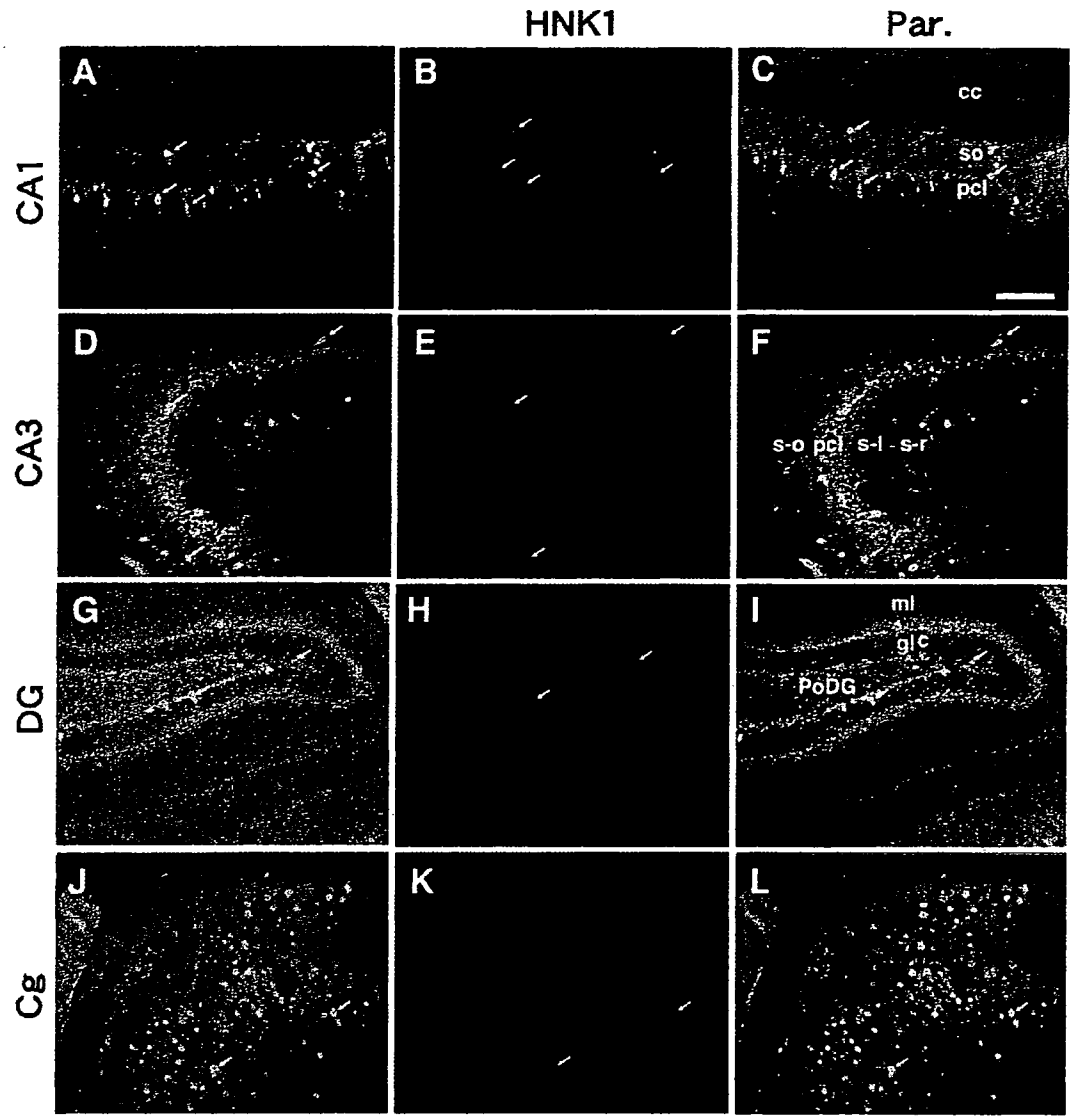

Fig. 5 – Double-labeled immunofluorescence micrographs with anti-HNK-1 (red) and anti-parvalbumin (green) antibodies in the CA1 subfield (A–C), the CA3 subfield (D–F), the dentate gyrus (G–I), and the cingulated cortex (J–L) of GlcAT-P-deficient mice. Scale bar=300 μm. Arrows show that HNK-1 signals were localized in neuronal cells containing parvalbumin.

cells expressed GlcAT-P mRNA and then the HNK-1 carbohydrate synthesis was catalyzed and projected to the molecular layer (Figs. 3E and F). Finally, the HNK-1 carbohydrate present in the LRt might have been brought there by fibers that arose from the cerebral cortex, the vestibular nuclei, and the hypothalamus, where GlcAT transcripts were expressed.

As shown in Fig. 2, the HNK-1 carbohydrate epitope widely distributed in most of brain disappeared in the GlcAT-P-deficient mice. However, HNK-1 immunoreactivity remained on neuronal cells in layers III to VI of cerebral cortex in the GlcAT-P-deficient mice (Figs. 2 and 3D). We have already reported that the remaining HNK-1 carbohydrate in the GlcAT-P-deficient mice corresponded to the perineuronal nets (Celio et al., 1998), which are known to comprise lattice-like accumulation of the extracellular matrix on a subset of neurons (Yamamoto et al., 2002). The major extracellur matrix of perineuronal nets are composed of hyaluronan, tenacin-R (Celio and Blumcke, 1994) and chondroitin sulfate proteoglycans such as neurocan, brevican, and phosphacan (Hagihara et al., 1999; Haunso et al., 1999; Matsui et al., 1998; Matthews et al., 2002; Rauch et al., 1991). It should be noted here that HNK-1 carbohydrate is expressed on most of extracellur matrix of perineuronal nets (Brückner et al., 2000). Furthermore, morphological alteration in *Wisteria floribunda* agglutinin (WFA)-labeled perineuronal nets around cortical interneurones in tenascin-R-deficient mice has been reported (Brückner et al., 2000). Then, to examine morphological alteration in *Wisteria*

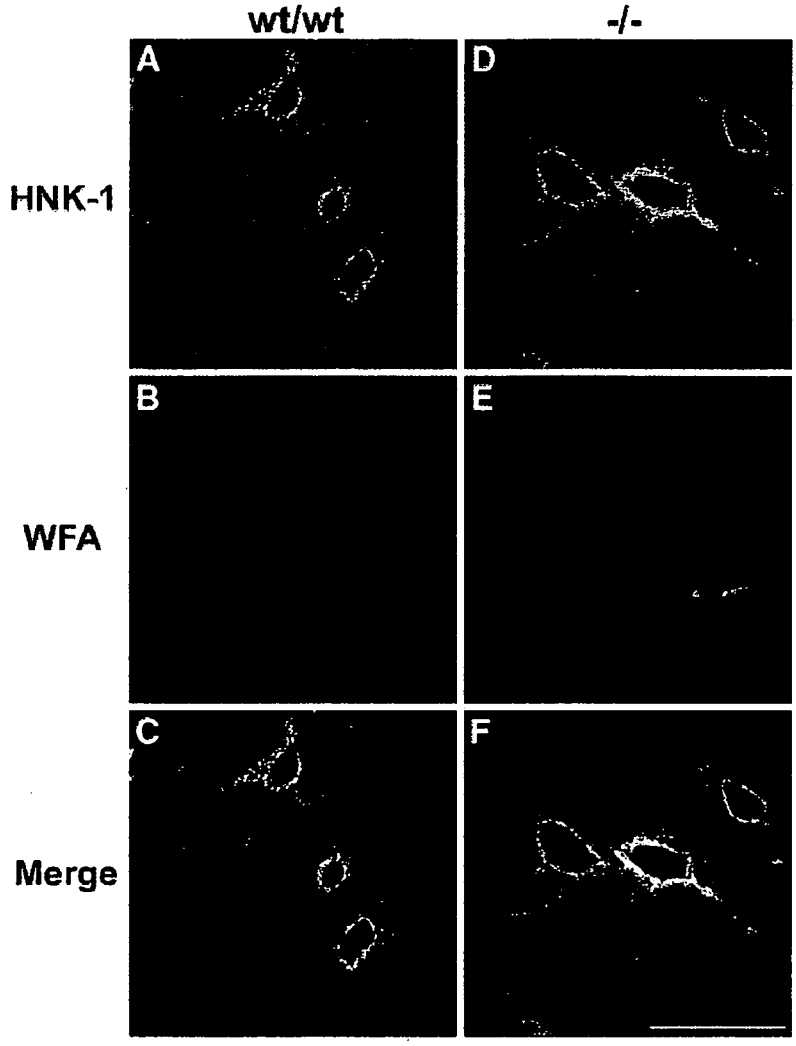

Fig. 6 – Double fluorescence staining focused on the perineuronal nets with anti-HNK-1 antibody (green) and WFA lectin (red). Brain coronal sections (40 μm thick) from 10-week-old wild-type (wt/wt; A–C) and GlcAT-P-deficient mice (–/–; D–F) were incubated with anti-HNK-1 antibody and WFA (*Wisteria Floribunda* agglutinin) lectin (SIGMA) and then incubated with FITC-conjugated anti-mouse IgM antibodies (zymed) and Rhodamine-conjugated avidin (vector). HNK-1 carbohydrate overlapping perineuronal net was found in GlcAT-P-deficient mice (F) as is the case with wild-type mice (C), and no obvious structural differences of perineuronal nets were observed in GlcAT-P-deficient mice at the fluorescence staining level. Scale bar=50 μm.

floribunda agglutinin (WFA)-labeled perineuronal nets in the GlcAT-P-deficient mice, we carried out double fluorescence staining with the HNK-1 antibody and WFA. As shown in Fig. 6, no obvious structural differences of perineuronal nets were observed in GlcAT-P-deficient mice at the fluorescence staining level, while perineuronal nets show clear structural changes in tenascin-R-deficient mice (Brückner et al., 2000). It suggests that the disappearance of HNK-1 carbohydrate in GlcAT-P-deficient mice has little effect on the formation of perineuronal nets. We are now trying to identify the molecular nature of the HNK-1 carbohydrate remaining in the perineuronal nets in GlcAT-P-deficient mice.

The present study was the first to show the regional relationship between GlcAT transcripts and the HNK-1 carbohydrate as an end-product in the brain, which will be very helpful for investigations of the role of HNK-1 carbohydrate in brain functions. Furthermore, this work provides the first example of histological enzyme-substrate analyses aimed at understanding the glycosylation system in the brain network.

4. Experimental procedure

4.1. Animals

Normal mice (8 weeks old and 45 weeks old, male; C57Bl/6J Jcl from CLEA Japan, Inc., Tokyo, Japan) and GlcAT-P-deficient mice (45 weeks old, male), which were backcrossed with

C57Bl/6J mice for more than eight generations, were utilized for experiments. All procedures were performed according to the guidelines for animal welfare of the Nara Institute of Science and Technology.

4.2. *In situ hybridization*

For preparation of riboprobes, the GlcAT-P and GlcAT-S target sequences were amplified using a single preparation of cDNA synthesized from hippocampal total RNA by one round of polymerase chain reaction using the following primers. The size of the final amplification product is shown in parentheses: GlcAT-P, 5'-TAG GGA GTA CTG CAT GTC CG -3'/5'-TAT AGT TGC GTG GTG TCT CT-3' (299 bp: nucleotide Nos. 488–786) and GlcAT-S, 5'-ACG CGC AGC GAG CTG GTG AG-3'/5'-TTT TGG ATT GGA CAA GAT GA-3' (417 bp: nucleotide Nos. 1019–1435). The polymerase chain reaction product was subcloned into pGEM-T easy vector. α ^{35}S-labeled riboprobes were prepared according to the manufacturer's instructions (Roche Molecular Biochemicals), using *Sal*I and T7 RNA polymerase (T7) for the antisense probe and *Nco*I and SP6 RNA polymerase (SP6) for the sense probe for GlcAT-P; and using *Nco*I and SP6 for the antisense probe and *Sal*I and T7 for the sense probe for GlcAT-S.

In situ hybridization histochemistry with [^{35}S]-labeled riboprobe (2×10^6 dpm/slide glass) was performed as described previously (Okabe et al., 2001). For tissue preparation, mice were anesthetized with diethyl ether inhalation and decapitated. Coronal sections (14-μm thick) were cut on a cryostat and thaw-mounted onto slides coated with 0.1% 3-aminopropyltriethoxy silane (Sigma-Aldrich, Tokyo, Japan) in acetone. Sections on slides were fixed in 4% formaldehyde in 0.1 M sodium phosphate, pH 7.4, for 20 min at room temperature. Next they were washed, treated with 10 μg/mL protease K in 50 mM Tris–HCl, pH 7.5, and 5 mM EDTA at room temperature for 3 min, postfixed with the above fixative, washed again, acetylated with 24 mM acetic anhydride and 0.1 M triethanolamine for 10 min, washed, then dehydrated through an ascending alcohol series. Each ^{35}S-labeled riboprobe (2×10^6 dpm/slide glass) was mixed with hybridization buffer; 50% deionized formamide, 0.3 M NaCl, 5 mM EDTA, 10% dextran sulfate, 1× Denhardt's solution, 0.2% *N*-lauroylsarcosine, 500 μg/mL yeast tRNA, 200 μg/mL salmon testis DNA, 2 mM dithiothreitol and 20 mM Tris–HCl, pH 8.0, placed on the sections, and incubated at 55 °C for 16 h. The sections were washed at 68 °C for 30 min each with 5× NaCl/Cit, 5 mm dithiothreitol and 50% formamide, 2× NaCl/Cit, 5 mm dithiothreitol. And they were treated with 2 μg/mL RNaseA in 0.5 M NaCl, 1 mM EDTA and 10 mM Tris–HCl, pH 7.5, at 37 °C for 30 min, then washed with 50% formamide, 2× NaCl/Cit, and 5 mM dithiothreitol at 68 °C for 30 min and with 2× NaCl/Cit and 0.1× NaCl/Cit at room temperature for 10 min each. After dehydration through an ascending alcohol series and air drying, slides were exposed to imaging plates (BAS2500, Fujifilm, Tokyo, Japan) for 24 h (macro-autoradiogram). The next day, slides were coated with autoradiography emulsion (NTB2, Kodak, Rochester, NY), exposed for 3 weeks, then developed with D-19 developer (Kodak) and fixed with Fuji fix (Fujifilm, Tokyo, Japan, Japan) in distilled water. The sections were observed under a light microscope with dark-field illumination (Nikon Corporation, Tokyo, Japan) (micro-autoradiogram), then sequentially stained with 0.01% thionine acetate (Nacalai Tesque, Inc., Kyoto, Japan) for observation under bright-field illumination. The specificity of the riboprobes was checked by comparing brain sections hybridized with sense and antisense probes. No signals were detected on the adjacent sections incubated in a control hybridization mixture containing sense probes corresponding to GlcAT cRNAs.

4.3. *Estimation of the regional distribution in normal mouse brain*

Pseudo color images of brains in macro-autoradiography (BAS2500) were produced using image analysis software (Win Roof v3.3, Mitani Corporation, Osaka Japan) to judge the differential intensity as described previously (Matsuhashi et al., 2003). Visual inspection of emulsion autoradiograms was also used to identify brain nuclei and particular cell types. Definitions for brain regions and nuclei were established following brain maps (Franklin and Paxinos, 1997). A combination analysis of macro- and micro-autoradiograms was used to establish the comparative distribution of the two transcripts, which was presented as a system of pluses (Table 1), with four pluses (++++) indicating maximal signal intensity. The hybridization patterns were virtually indistinguishable between mice ($n=3$) and among independent hybridizations (≥ 2).

4.4. *Quantification of signal intensity of GlcAT transcripts in the CA3 subfield of the hippocampal formation in microautoradiography*

The signal intensities in sections cut at −2.0 mm with respect to the bregma were examined. The signal intensity within a ϕ175.25 μm^2 circular field in the CA3 subfield under dark-field illumination was measured automatically using Win Roof v3.3 ($n=8$). The raw signal intensity of a circle in the isocortex was taken background in each section. Figs. 4A–D shows representative fields among images used for the analyses.

4.5. *Immunohistochemistry*

Mice (45weeks old) were perfused under deep anesthesia through the heart with 4% paraformaldehyde in 0.1 M sodium phosphate, pH 7.4. Brains were removed, kept in the same fixative at 4 °C for 16 h and in 30% sucrose, 0.1 M sodium phosphate, pH 7.4, at 4 °C for 48 h, frozen on dry ice, and sectioned coronally at 30 μm on a cryostat.

Immunohistochemical analysis was performed with mouse monoclonal HNK-1 antibody (American Type Culture Collection) and then the anti-mouse IgM antibody conjugated with horseradish peroxidase (HRP). Sections were developed with 0.02% 3,3'-diaminobenzidine (Wako Pure Chemical Industries, Ltd., Osaka, Japan) in 50 mM Tris–HCl, pH 7.6, 0.6% ammonium nickel (II) sulfate hexahydrate (Wako Pure Chemical Industries), and 0.01% hydrogen peroxide. Images were captured with an Axioplan 2 (Carl Zeiss, Tokyo, Japan). For double-labeled immunofluorescence histochemistry, the sections were incubated with biotinylated HNK-1 antibody and mouse

monoclonal anti-parvalbumin (Swant, 235, Bellinzona, Switzerland) as primary antibodies and then with rhodamine–avidin and anti-mouse IgG antibody conjugated with fluorescein isothiocyanate (BIOSOURCE International, CA, USA) as secondary antibodies. Images were captured with a laser scanning microscope (LSM510 invert; Carl Zeiss, Tokyo, Japan). The immunohistochemical patterns were virtually indistinguishable between mice ($n=3$) and among independent reactions (≥ 3).

Acknowledgments

This work was partly supported by grants from the Ministry of Education, Science, Culture, and Sports (13680843 to K.K.). This work was also supported in part by a Grant-in-Aid for Creative Scientific Research (16GS0313 to S.O.) and a Grant-in-Aid for Scientific Research on Priority Areas (A-14082203 to T.K.) from the Ministry of Education, Culture, Sports and Technology.

REFERENCES

Brückner, G., Grosche, J., Schmidt, S., Härtig, W., Margolis, R.U., Delpech, B., Seidenbecher, C.I., Czaniera, R., Schachner, M., 2000. Postnatal development of perineuronal nets in wild-type mice and in a mutant deficient in tenascin-R. J. Comp. Neurol. 428, 616–629.

Butcher, L.L., 1995. Cholinergic neurons and networks, In: Paxinos, G. (Ed.), The Rat Nervous System, second edition. Academic Press Inc., San Diego, pp. 1003–1015.

Butcher, L.L., Woolf, N.J., 2004. Cholinergic neurons and networks revisited, In: Paxinos, G. (Ed.), The Rat Nervous System, third edition. Academic Press Inc., San Diego, pp. 1257–1268.

Celio, M.R., Blumcke, I., 1994. Perineuronal nets: a specialized form of extracellular matrix in the adult nervous system. Brain Res. Rev. 19, 128–145.

Celio, M.R., Spreafico, R., Biasi, S., Vitellaro-Zuccarello, L., 1998. Perineuronal nets: past and present. Trends Neurosci. 21, 510–515.

Chou, D.K.H., Ilyas, A.A., Evans, J.E., Costello, C., Quarles, R.H., Jungalwala, F.B., 1986. Structure of sulfated glucuronyl glycolipids in the nervous system reacting with HNK-1 antibody and some IgM paraproteins in neuropathy. J. Biol. Chem. 261, 11717–11725.

Dityatev, A., Schachner, M., 2003. Extracellular matrix molecules and synaptic plasticity. Nat. Rev., Neurosci. 4, 456–468.

Franklin, K.B.J., Paxinos, G., 1997. The Mouse Brain in Stereotaxic Coordinates. Academic Press Inc., San Diego.

Groenewegen, H.J., Witter, M.P., 2004. Thalamus, In: Paxinos, G. (Ed.), The Rat Nervous System, third edition. Academic Press Inc., pp. 407–453.

Hagihara, K., Miura, R., Kosaki, R., Berglund, E., Ranscht, B., Yamaguchi, Y., 1999. Immunohistochemical evidence for the brevicantenascin-R interaction: colocalization in perineuronal nets suggests a physiological role for the interaction in the adult rat brain. J. Comp. Neurol. 410, 256–264.

Haunso, A., Celio, M.R., Margolis, R.K., Menoud, P.A., 1999. Phosphacan immunoreactivity is associated with perineuronal nets around parvalbumin-expressing neurones. Brain Res. 834, 219–222.

Kakuda, S., Sato, Y., Tonoyama, Y., Oka, S., Kawasaki, T., 2005. Different acceptor specificities of two glucuronyltransferases involved in the biosynthesis of HNK-1 carbohydrate. Glycobiology 15, 203–210.

Kosaka, T., Katsumaru, H., Hama, K., Wu, J.Y., Heizmann, C.W., 1987. GABAergic neurons containing the Ca2+-binding protein parvalbumin in the rat hippocampus and dentate gyrus. Brain Res. 419, 119–130.

Kosaka, T., Isogai, K., Barnstable, C.J., Heizmann, C.W., 1990. Monoclonal antibody HNK-1 selectively stains a subpopulation of GABAergic neurons containing the calcium-binding protein parvalbumin in the rat cerebral cortex. Exp. Brain Res. 82, 566–574.

Kosaka, T., Heizmann, C.W., Fujita, S.C., 1992. Monoclonal antibody 473 selectively stains a population of GABAergic neurons containing the calcium-binding protein parvalbumin in the rat cerebral cortex. Exp. Brain Res. 89, 109–114.

Kruse, J., Maihammer, R., Werneche, H., Faissner, A., Sommer, I., Goridis, C., Schachner, M., 1984. Neural cell adhesion molecules and myelin-associated glycoprotein share a common carbohydrate moiety recognized by monoclonal antibodies L2 and HNK-1. Nature 311, 153–155.

Kruse, J., Keilhauer, G., Faissner, A., Timpl, R., Schachner, M., 1985. The J1 glycoprotein—A novel nervous system cell adhesion molecule of the L2/HNK-1 family. Nature 316, 146–148.

Kunemund, V., Jungalwala, F.B., Fischer, G., Chou, D.K., Keilhauer, G., Schachner, M., 1988. The L2/HNK-1 carbohydrate of neural cell adhesion molecules is involved in cell interactions. J. Cell Biol. 106, 213–223.

Malmierca, M.S., Merchán, M.A, 2004. Auditory system, In: Paxinos, G. (Ed.), The Rat Nervous System, third edition. Academic Press Inc., San Diego, pp. 997–1082.

Martini, R., Xin, Y., Schumitz, B., Schachner, M., 1992. The L2/HNK-1 carbohydrate epitope is involved in the preferential outgrowth of motor neuron on ventral roots and motor nerves. Eur. J. Neurosci. 4, 628–639.

Matsuhashi, H., Horii, Y., Kato, K., 2003. Region-specific and epileptogenic-dependent expression of six subtypes of alpha2,3-sialyltransferase in the adult mouse brain]. J. Neurochem 84, 53–66.

Matsui, F., Nishizuka, M., Yasuda, Y., Aono, S., Watanabe, E., Oohira, A., 1998. Occurrence of a N-terminal proteolytic fragment of neurocan, not a C-terminal half, in a perineuronal net in the adult rat cerebrum. Brain Res. 790, 45–51.

Matthews, R.T., Kelly, G.M., Zerillo, C.A., Gray, G., Tiemeyer, M., Hockfield, S., 2002. Aggrecan glycoforms contribute to the molecular heterogeneity of perineuronal nets. J. Neurosci. 22, 7536–7547.

Okabe, A., Tawara, Y., Masa, T., Oka, T., Machida, A., Tanaka, T., Matsuhashi, H., Shiosaka, S., Kato, K., 2001. Differential expression of mRNAs for sialyltransferase isoenzymes induced in the hippocampus of mouse following kindled seizures. J. Neurochem. 77, 1185–1197.

Ong, E., Suzuki, M., Belot, F., Yeh, J.C., Franceschini, I., Angata, K., Hindsgaul, O., Fukuda, M., 2002. Biosynthesis of HNK-1 glycans on O-linked oligosaccharides attached to the neural cell adhesion molecule (NCAM): the requirement for core 2 beta 1,6-N-acetylglucosaminyltransferase and the muscle-specific domain in NCAM. J. Biol. Chem. 277, 18182–18190.

Pizzorusso, T., Medini, P., Berardi, N., Chierzi, S., Fawcett, J.W., Maffei, L., 2002. Reactivation of ocular dominance plasticity in the adult visual cortex. Science 298, 1187–1189.

Rauch, U., Gao, P., Janetzko, A., Flaccus, A., Hilgenberg, L., Tekotte, H., Margolis, R.K., Margolis, R.U., 1991. Isolation and characterization of developmentally regulated chondroitin sulfate and chondroitin/keratan sulfate proteoglycans of brain identified with monoclonal antibodies. J. Biol. Chem. 266, 14785–14801.

Rhodes, K.E., Fawcett, J.W., 2004. Chondroitin sulphate proteoglycans: preventing plasticity or protecting the CNS? J. Anat. 204, 33–48.

Risold, P.Y., 2004. The septal region, In: Paxinos, G. (Ed.), The Rat Nervous System, third edition. Academic Press Inc., San Diego, pp. 605–632.

Ruigrok, T.J.H., 2004. Precerebellar nuclei and red nucleus, In: Paxinos, G. (Ed.), The Rat Nervous System, third edition. Academic Press Inc., San Diego, pp. 167–204.

Saghatelyan, A.K., Gorissen, S., Albert, M., Hertlein, B., Schachner, M., Dityatev, A., 2000. The extracellular matrix molecule tenascin-R and its HNK-1 carbohydrate modulate perisomatic inhibition and long-term potentiation in the CA1 region of the hippocampus. Eur. J. Neurosci. 12, 3331–3342.

Seiki, T., Oka, S., Terayama, K., Imiya, K., Kawasaki, T., 1999. Molecular cloning and expression of a second glucuronyltransferase involved in the biosynthesis of the HNK-1 carbohydrate epitope. Biochem. Biophys. Res. Commun. 255, 182–187.

Shimoda, Y., Tajima, Y., Nagase, T., Harii, K., Osumi, N., Sanai, Y., 1999. Cloning and expression of a novel galactoside beta1, 3-glucuronyltransferase involved in the biosynthesis of HNK-1 epitope. J. Biol. Chem. 11, 17115–17122 (Erratum in: J Biol Chem 274, 21490).

Simerly, R.B., 2004. Anatomical substrates of hypothalamic integration, In: Paxinos, G. (Ed.), The Rat Nervous System, third edition. Academic Press Inc., San Diego, pp. 335–368.

Terayama, K., Oka, S., Seiki, T., Miki, Y., Nakamura, A., Kozutsumi, Y., Takio, K., Kawasaki, T., 1997. Cloning and functional expression of a novel glucuronyltransferase involved in the biosynthesis of the carbohydrate epitope HNK-1. Proc. Natl. Acad. Sci. U. S. A. 94, 6093–6098.

Terayama, K., Seiki, T., Nakamura, A., Matsumori, K., Ohta, S., Oka, S., Sugita, M., Kawasaki, T., 1998. Purification and characterization of a glucuronyltransferase involved in the biosynthesis of the HNK-1 epitope on glycoproteins from rat brain. J. Biol. Chem. 273, 30295–30300.

Tracey, D., 2004. Somatosensory system, In: Paxinos, G. (Ed.), The Rat Nervous System, third edition. Academic Press Inc., San Diego, pp. 797–815.

Voshol, H., van-Zuylen, C.W., Orberger, G., Vliegenthart, J.F., Schachner, M., 1996. Structure of the HNK-1 carbohydrate epitope on bovine peripheral myelin glycoprotein P0. J. Biol. Chem. 271, 22957–22960.

Yamamoto, M., Marshall, P., Hemmendinger, L.M., Boyer, A.B., Caviness Jr., V.S, 1988. Distribution of glucuronic acid-and-sulfate-containing glycoproteins in the central nervous system of the adult mouse. Neurosci. Res. 5, 273–298.

Yamamoto, S., Oka, S., Inoue, M., Shimuta, M., Manabe, T., Takahashi, H., Miyamoto, M., Asano, M., Sakagami, J., Sudo, K., Iwakura, Y., Ono, K., Kawasaki, T., 2002. Mice deficient in nervous system-specific carbohydrate epitope HNK-1 exhibit impaired synaptic plasticity and spatial learning. J. Biol. Chem. 277, 27227–27231.

Waite, P.M.E., 2004. Trigeminal sensory system, In: Paxinos, G. (Ed.), The Rat Nervous System, third edition. Academic Press Inc., San Diego, pp. 817–851.

Zamze, S., Wing, D.R., Wormald, M.R., Hunter, A.P., Dwek, R.A., Harvey, D.J., 2001. A family of novel, acidic N-glycans in Bowes melanoma tissue plasminogen activator have L2/HNK-1-bearing antennae, many with sulfation of the fucosylated chitobiose core. Eur. J. Biochem. 268, 4063–4078.

Available online at www.sciencedirect.com
ScienceDirect
Journal of Controlled Release 118 (2007) 303–309
journal of controlled release
www.elsevier.com/locate/jconrel

Effective tumor regression by anti-neovascular therapy in hypovascular orthotopic pancreatic tumor model

Sei Yonezawa, Tomohiro Asai, Naoto Oku *

Department of Medical Biochemistry and COE Program in the 21st Century, University of Shizuoka School of Pharmaceutical Sciences, 52-1 Yada, Suruga-ku, Shizuoka 422-8526, Japan

Received 10 September 2006; accepted 21 December 2006
Available online 5 January 2007

Abstract

Pancreatic cancer is one of the most serious cancers with poor therapeutic results and prognosis. In here, we proposed a novel treatment strategy of pancreatic cancer by injuring limited angiogenic vessels with liposome containing adriamycin. At first, we established an orthotopic tumor model, which has a hypovascular characteristic of pancreatic tumor. In this model, we obtained the enhanced therapeutic efficacy with liposome that modified by polyethylene glycol (PEG) and a peptide, Ala-Pro-Arg-Pro-Gly (APRPG), having an affinity to neovessels. Histochemical analysis suggested the degradation of angiogenic vessels after treatment with APRPG-PEG-liposomal adriamycin. In addition, we observed colocalization of fluorescence-labeled APRPG-PEG-liposome with angiogenic endothelial cells, although the biodistribution of ^{3}H-labeled liposome did not show the difference in the amount of accumulation between PEG-modified liposome and APRPG-PEG-modified liposome. These results suggested the availability of the anti-neovascular therapy against pancreatic cancer and supply a new sight indication on chemotherapeutics against pancreatic cancer.
© 2007 Elsevier B.V. All rights reserved.

Keywords: Anti-neovascular therapy; Liposome; Pancreatic cancer; Angiogenesis

1. Introduction

Pancreatic cancer is one of the most difficult cancers to control: This cancer is difficult to diagnose, and shows high malignant potential. Five-year survival of patients suffering pancreatic cancer is less than 5% in the United States, Japan and Europe, and the incidence rate of it is equal to the death rate [1]. Therefore, it is suggested that existing chemotherapeutics have a limitation of the effect on pancreatic cancer, and an effective treatment modality is awaited. It is interesting to note that pancreatic cancer has less vasculature in number than other cancers such as breast or colorectal cancer known as vasculature-rich cancers. In computed tomography (CT) and magnetic resonance imaging (MRI), pancreatic tumor is considered as a hypovascular lesion compared to normal pancreatic tissue [2–4]. This property can be thought as the reason why effective pancreatic tumor chemotherapy cannot be expected due to the low bioavailability of the chemotherapeutic drugs.

On the other hand, angiogenic vessels are known to play an important role in pancreatic tumor progression as well as other tumors [5]. In general, anti-angiogenic therapy is thought to be effective for cancer treatment. Actually, many anti-angiogenic therapies that inhibit the certain steps of angiogenesis have examined. For example, matrix metalloproteinase inhibitors and anti-vascular endothelial growth factor (VEGF) agents etc., have been developed [6–8]. However, they are thought to be limited for the induction of tumor dormancy [9,10]. We previously proposed a novel therapeutic strategy targeted angiogenic vessels, cancer anti-neovascular therapy (ANET), that kills the proliferative endothelial cells followed by indirect induction of tumor regression [11,12]. Neovessel endothelial cells are growing, so it can be thought that these cells are susceptible to anti-cancer drugs like tumor cells. The benefits that can be gained from ANET are not only the effective tumor treatment but also the inhibition of tumor hematogenous metastasis, the avoidance of drug resistance, and wide range of application

* Corresponding author. Tel.: +81 54 264 5701; fax: +81 54 264 5705.
E-mail address: oku@u-shizuoka-ken.ac.jp (N. Oku).

0168-3659/$ - see front matter © 2007 Elsevier B.V. All rights reserved.
doi:10.1016/j.jconrel.2006.12.024

against many kinds of tumors. For ANET, we previously isolated APRPG peptide from a phage-displayed peptide library by biopanning of phage clones specifically bound to tumor angiogenic vasculature. *In vitro* study, we observed higher uptake of APRPG-modified liposome in human umbilical vein endothelial cells (HUVECs) than non-modified one. Furthermore, higher accumulation of APRPG-modified liposomes in tumor tissue than non-modified one was also observed in tumor-bearing mice [12].

In here, we carried out a series of experiments focused on the application of ANET to pancreatic tumor model, since it is thought that ANET is more effective in hypovascular tumors than hypervascular tumors. Firstly, we established hypovascular orthotopic pancreatic tumor model, following the investigation of biodistribution of angiogenic vessel-targeted liposome in the tumor-bearing mice. In this experiment, we used APRPG-polyethyleneglycol (PEG)-modified liposome as the angiogenic vessel-targeted liposome. Modification by PEG is known to protect liposomes from opsonization and contact with lipoproteins through the formation of aqueous layers on the surface of liposomes. Thus, the APRPG-PEG-modified liposome could have long-circulating characteristic, and would have more chance to contact with neovasculature. Next, we examined the intratumoral distribution of liposomes by using confocal laser scan microscopy. And finally, we treated the orthotopic pancreatic tumor model with APRPG-PEG-modified liposomes encapsulating adriamycin (ADM) and evaluated the therapeutic effect. The obtained data indicated that ANET is effective for pancreatic tumor treatment.

2. Materials and methods

2.1. Materials

Distearoylphosphatidylcholine (DSPC) and distearoylphosphatidylethanolamine (DSPE) were kindly gifted form Nippon Fine Chemical Co., Ltd. (Hyogo, Japan). PEG-APRPG-conjugated DSPE (DSPE-PEG-APRPG) and PEG-conjugated DSPE (DSPE-PEG) were prepared as described previously [13]. Cholesterol was purchased from Sigma (St. Louis, MO, USA). All other reagents used were the analytical grades.

2.2. Cell culture

Human pancreatic cancer cell line SUIT-2 was generously donated by Dr. Haruo Iguchi (National Kyushu Cancer Center, Fukuoka, Japan). SUIT-2 cells were cultured in RPMI 1640 supplemented with streptomycin, penicillin, and 10% fetal bovine serum (FBS, Sigma) at 37 °C in a humidified atmosphere containing 5% CO_2.

2.3. Orthotopic tumor model

BALB/c nude mice were anesthetized by intraperitoneal injection of pentobarbital (Dainippon Sumitomo Pharmaceutical Co., Ltd. Osaka, Japan). After cutting abdomen of a mouse, pancreas was exteriorized and dilated on its belly sterilized by chlorhexidine gluconate solution. Then 20 μL of SUIT-2 cells (5×10^6 cells/mouse) were injected into pancreas. Then cut area was sutured and sterilized by chlorhexidine gluconate solution.

2.4. Histopathological examination

SUIT-2 cells (5×10^6 cells/mouse) were inoculated as described in the Section 2.3. At day 3 and 9 after tumor implantation, mice were sacrificed and tumor was dissected. The tumor was embedded in optimal cutting temperature compound (Sakura Finetechnochemical Co., Ltd., Tokyo, Japan) and frozen at −80 °C. Nine-micrometer tumor sections were prepared by using cryostatic microtome (HM 505E, Microm, Walldorf, Germany), mounted on MAS coated slides (Matsunami Glass Ind., Ltd., Japan), and air-dried for 1 h. The tumor tissue sections prepared were stained with hematoxylin-eosin and histopathological examination was performed.

2.5. Evaluation of micro vessel density (MVD) in pancreatic tumor model

SUIT-2 cells (5×10^6 cells/mouse) were inoculated as described in the Section 2.3. On the day 10 and 25 after tumor implantation, mice were sacrificed and the tumor section was prepared as described in the Section 2.4. The tumor tissue sections prepared were fixed in acetone for 10 min at room temperature, washed twice with phosphate-buffered saline (PBS), pH 7.4, (5 min each time), and incubated with protein-blocking solution containing 1% bovine serum albumin in PBS for 10 min at room temperature. Then, the samples were incubated with an appropriately diluted (1:50) biotinylated anti-mouse CD31 rat monoclonal antibody (Becton Dickinson Lab., Franklin Lakes, NJ, USA) for 18 h at 4 °C. After the sections were rinsed thrice (2 min each time) with PBS, they were incubated with streptavidin-Alexa fluor® 488 conjugates (Molecular Probes Inc., Eugene, OR, USA) for 30 min at room temperature in a humid chamber. Samples were washed twice with PBS (2 min each time). Finally, sections were counterstained and mounted with Perma Fluor Aqueous Mounting Medium (Thermo Shandon, Pittsburgh, PA, USA). These sections were fluorescently observed by using microscopic LSM system (Carl Zeiss, Co., Ltd.): Endothelial cells were identified as green fluorescence. Hot spot area of the samples and CD31 positive area were quantified by ImageJ software to obtain micro vessel density (MVD). For immunostaining, the sections treated with biotinylated anti-mouse CD31 rat monoclonal antibody were stained with VECTASTAIN® ABC Kit (Vector Laboratories, Inc., Burlingame, CA, USA) by using diaminobenzidine tetrahydrochloride (DAB, Funakoshi Co., Ltd., Tokyo, Japan) as a colorimetric substrate. Then the sections were rinsed with PBS and co-stained with hematoxylin.

2.6. Preparation of liposomes

Liposomes composed of DSPC and cholesterol with DSPE-PEG or DSPE-PEG-APRPG (10:5:1 as a molar ratio, PEG-Lip and APRPG-PEG-Lip, respectively) were prepared as described

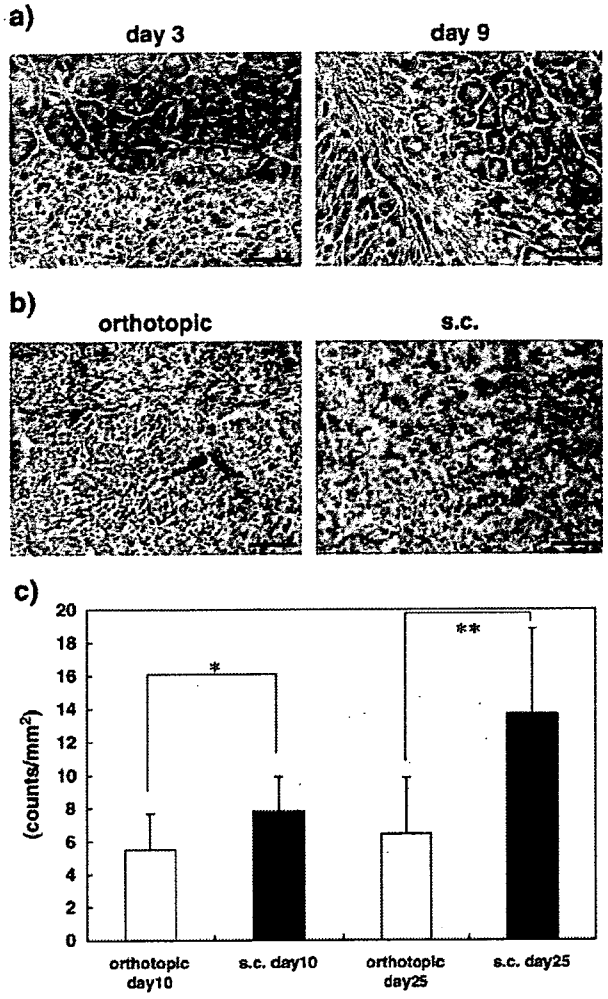

Fig. 1. Characteristics of orthotopic pancreatic tumor model. SUIT-2 cells (5×10^6 cells) were implanted into the pancreas of BALB/c nude mice. At day 3 and 9 after the tumor implantation, mice were sacrificed and tumor sections were prepared as described in Materials and methods. Then they were stained with hematoxylin and eosin (a). On the day 10 and 25, tumor sections were also prepared for evaluating vasuclarization. The sections were immunostained with biotinylated anti-mouse CD31 monoclonal antibody, and visualized with DAB as colorimetric substarate (b) or streptavidin-Alexa fluor® 488 conjugated-second antibody. CD31 positive area was observed fluorescently by a laser scanning microscopy and was quantified by ImageJ software (c). Significant differences are shown with asterisks: *, $p<0.05$ and **, $p<0.01$. Scale bar represents 100 μm.

previously [14]. In brief, lipids were dissolved in chloroform or chloroform/methanol, dried under reduced pressure, and stored *in vacuo* for at least 1 h. Then, the liposomes were formed by hydration of the thin lipid film with 0.3 M glucose, and frozen and thawed for 3 cycles using liquid nitrogen. Then liposomes were sized by thrice extrusion through a polycarbonate membrane filter with 100-nm pores. For a biodistribution study, a trace amount of [^{3}H]-cholesterylhexadecylether (Amersham Pharmacia, Buckinghamshire, UK) was added to the initial chloroform/methanol solution as described above. To observe the intratumoral distribution of liposomes, they were fluorescently labeled with 1,1′-dioctadecyl-3, 3, 3′, 3′-tetramethylindocarbocyanine perchlorate (DiI C_{18}; Molecular Probes Inc., Eugene, OR, USA), which was added to them at the quantity equivalent to 1 mol% of DSPC. For therapeutic experiment, ADM-encapsulated liposome was prepared by a modification of the remote-loading method as described previously [14]. The concentration of ADM was determined at 484 nm absorbance.

2.7. Biodistribution of liposome

Biodistribution study was performed at day 10 after SUIT-2 tumor implantation. Orthotopic pancreatic tumor model mice were injected with radiolabeled liposomes containing [^{3}H] cholesterylhexadecylether *via* a tail vein. Three or twenty-four hours after injection, the mice were sacrificed under diethyl ether anesthesia for the collection of the blood. Then the blood was centrifuged (600 ×*g* for 5 min) to obtain the plasma. After the mice had been bled from the carotid artery, the heart, lung, liver, spleen, kidney and tumor were removed, washed with saline and weighed. The radioactivity in each organ as well as plasma was determined with a liquid scintillation counter (Aloka LSC-3100). Distribution data are presented as % dose per 100-mg wet tissue, where the total amount in plasma was calculated based on the average mice body weight, which was 25.5 g and average plasma volume, which was assumed to be 4.27% of body weight based on the data of total blood volume. The animals were cared for according to the animal facility guidelines of the University of Shizuoka.

2.8. Intratumoral distribution of liposome

DiI C_{18}-labeled liposomes were administered *via* a tail vein of mice with orthotopic pancreatic tumor on the day 3, 9 and 18

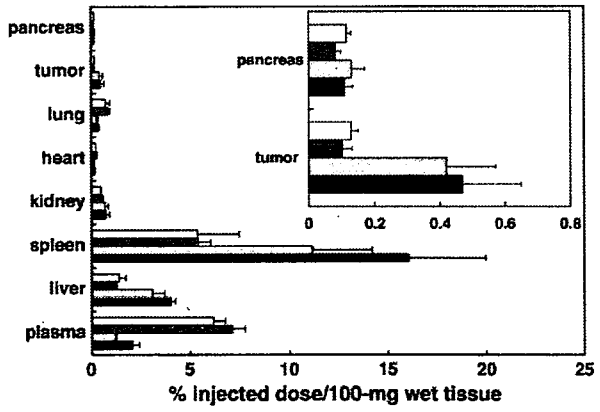

Fig. 2. Biodistribution of ^{3}H-labeled liposomes in various organs. Orthotopic pancreatic tumor model mice were injected with ^{3}H-labeled-PEG-modified liposome or APRPG-PEG-modified liposome *via* a tail vein at day 10 after tumor implantation. Three and twenty-four hours after injection, mice were dissected and the radioactivity in each organ was determined ($n=3$). Data are presented as percent of the injected dose per 100 mg tissue and S.D. Inset indicates the liposomal accumulation in the tumor and in pancreas represented as the percent-injected dose per 100 mg wet tissue. Data represents 3 h PEG-Lip (open bar), 3 h APRPG-PEG-Lip (dark gray bar), 24 h PEG-Lip (light gray bar) and 24 h APRPG-PEG-Lip (closed bar), respectively.

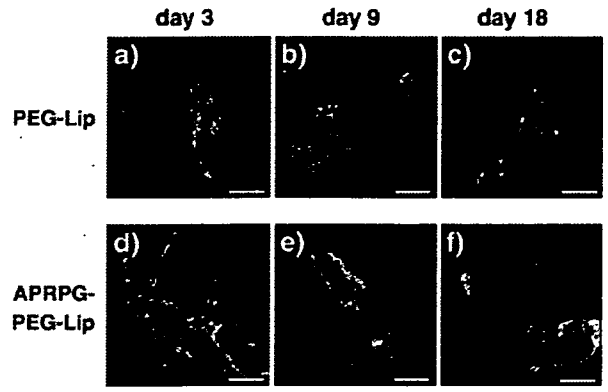

Fig. 3. Intratumoral distribution of $DiIC_{18}$-labeled liposomes. Orthotopic pancreatic tumor model mice were injected with PEG-Lip (a–c) or APRPG-PEG-Lip (d–f) labeled with $DiIC_{18}$ *via* a tail vein at day 3 (a, d), day 9 (b, e), and day 18 (c, f) after tumor implantation. At 2 h after injection of fluorescence-labeled liposomes, frozen-sections of each tumor were prepared. Green portions indicate CD31-positive regions, red portions liposomal distribution, and yellow portions show the localization of liposomes at the site of vascular endothelial cells. Scale bar represents 50 μm.

after tumor implantation. Two hours after injection of liposomes, mice were sacrificed under diethyl ether anesthesia and the tumor was dissected. Preparation of tumor sections and CD31 staining were performed as described in the Section 2.5. These tumor sections were fluorescently observed by using microscopic LSM system (Carl Zeiss, Co., Ltd.): Endothelial cells were identified as green fluorescence and liposomes were detected as red.

2.9. Therapeutic experiment

Orthotopic pancreatic tumor model was prepared by the injection of SUIT-2 cells (5×10^6 cells/mouse). Liposomes encapsulating ADM or 0.3 M glucose solution were administered intravenously into SUIT-2-bearing mice at day 3, 6, 9 and 12 after the tumor cell implantation. The injected dose of liposomal ADM in each administration was 10 mg/kg as ADM. The weight of tumor was examined at day 15. For histochemical analysis, the sections of tumor were prepared, and then immunostaining with anti-CD31 antibody and hematoxylin-eosin staining were performed as described above.

2.10. Statistical analysis

Student's *t*-test was used for statistical analysis, and $p<0.05$ were considered to be statistically significant.

3. Results

3.1. Preparation of orthotopic pancreatic tumor model

At first, we examined the characteristics of orthotopic pancreatic tumor model by using SUIT-2 human pancreatic tumor cell line. Histopathological examination indicated that tumor cells invaded into neighboring pancreatic tissue at 3 and 9 days after tumor implantation (Fig. 1a). Then we investigated whether the model showed hypovascular characteristics or not. For this purpose, vascular density of the model was compared with that of s.c. implanted SUIT-2 tumor model. The result of immunostaining with anti-CD31 antibody showed that MVD of orthotopic pancreatic tumor model was lower than that of s.c. implanted model (Fig. 1b): The significant differences were observed in CD31 positive area of day 10-orthotopic model mice from that of day 10-s.c. model mice ($p<0.05$), day 25-orthotopic model mice from day 25-s.c. model mice ($p<0.01$). These data indicated that orthotopic implantation of SUIT-2 cells developed pancreatic tumor with hypovascular characteristics. The immunostaining study also confirmed the hypovascular characteristics of the orthotopic pancreatic tumor model (Fig. 1c).

3.2. Biodistribution of liposomes

Before therapeutic experiment, we investigated the biodistribution of the liposome in the orthotopic pancreatic tumor-bearing mice, since the accumulation of drug carrier is prerequisite for the therapeutic effect of entrapped drugs in the carrier at the target site. Ten days after SUIT-2 tumor implantation, ^{3}H-labeled PEG-Lip or APRPG-PEG-Lip was injected *via* a tail vein. Three and twenty-four hours after injection of liposomes, mice were sacrificed and tumor and other organs were dissected for measuring the radioactivity in these tissues. Both PEG-Lip and APRPG-PEG-Lip accumulated in tumor time-dependently, although there was no significant difference between those two kinds of liposomes (Fig. 2). Therefore, even though in the hypovascular tumor, enhanced permeability and retention (EPR) effect of liposomes is achieved to some extent.

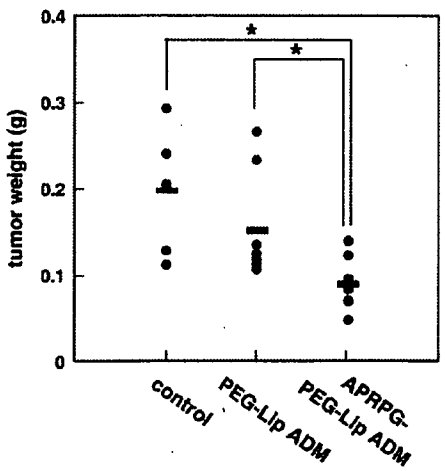

Fig. 4. Therapeutic effect of APRPG-PEG-modified liposome encapsulating ADM on orthotopic pancreatic tumor model mice. Orthotopic pancreatic tumor model mice were injected *i.v.* with 0.3 M Glucose (control), PEG-LipADM or APRPG-PEG-LipADM for 4 times at day 3, 6, 9 and 12 after tumor implantation ($n=6$–8). Injected dose of liposomal ADM were adjusted to 10 mg/kg as ADM concentration in each time. The weight of the tumors was measured at day 15. Significant differences are shown with asterisks: *, $p<0.05$.

3.3. Intratumoral distribution of liposomes

Next, we determined intratumoral distribution of the liposomes in the present hypovascular tumor model. Three, nine and 18 days after tumor implantation, DiI C_{18}-labeled liposomes were injected *via* a tail vein of SUIT-2 orthotopically implanted mice. Two hours after injection, frozen section of tumor was prepared. After fluoroimmunostaing with CD31 antibody, the intratumoral distribution of liposomes was observed with confocal laser scan microscopy. As shown in Fig. 3a–c, red fluorescence indicating PEG-Lip localization was observed in vascular like structure of CD31-staining (green fluorescence). On the contrary, fluorescence of APRPG-PEG-Lip was observed not only in the vessel like structure but also with CD31-staining, suggesting that APRPG-PEG-Lip was associated with angiogenic endothelial cells.

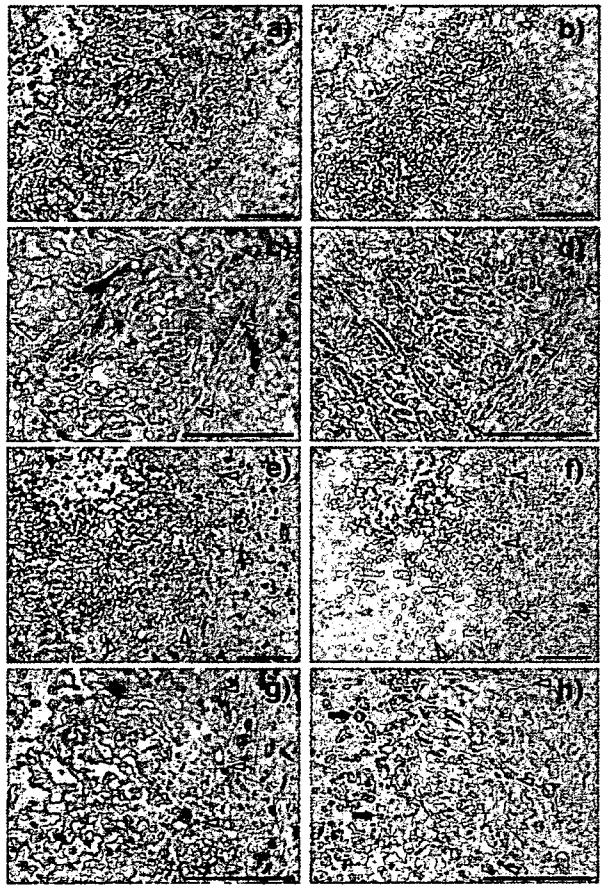

Fig. 5. Immunohistochemical analysis of dissected tumor after the treatment tumor model mice with APRPG-PEG-modified liposome encapsulating ADM. Orthotopic pancreatic tumor model mice were treated as described in the legend of Fig. 4. Tumor sections were prepared from the mice treated with PEG-LipADM (a–d) or with APRPG-PEG-LipADM (e–h). The sections were immunostained with biotinylated anti-mouse CD31 monoclonal antibody and visualized with DAB, and then co-stained with hematoxylin (a, c, e, g), or stained with hematoxylin-eosin (b, d, f, h). Arrowheads indicate the boundary of normal and tumor tissues, and arrows in (h) indicate macrophages. Scale bar represents 100 μm.

3.4. Therapeutic experiment by use of ADM-loaded liposomes

To examine the therapeutic effect of neovessel-targeted liposomal ADM on the orthotopic pancreatic tumor model mice, ADM-encapsulated APRPG-PEG-modified liposome (APRPG-PEG-LipADM) or ADM-encapsulated PEG-modified liposome (PEG-LipADM) were injected *via* a tail vein of the mice at 3, 6, 9 and 12 days after the tumor implantation. At day 15, tumor was removed and weighed to evaluate the effect of the treatment. As shown in Fig. 4, the significant differences in tumor weight of APRPG-PEG-LipADM-treated group from control ($p<0.05$) and PEG-LipADM-treated group ($p<0.05$) were observed. We also examined the body weight change of these mice after tumor implantation as an indicator of side effects, and observed that no significant difference between the three groups tested (data not shown).

Finally the sections of dissected tumor tissues were examined by immunostaining of CD31 and hematoxylin-eosin staining. As shown in Fig. 5, CD31-positive cells were observed in the tumor to some extent after treatment with PEG-LipADM. On the contrary, vessel-like structures were disappeared in the tumor after treatment with APRPG-PEG-LipADM, suggesting that APRPG-PEG-LipADM degenerated neovessels inside the tumor. Furthermore, the invasion of macrophages into the tumor was observed in the latter case.

4. Discussion

General anti-angiogenic therapy is based on the inhibition of the angiogenic cascade such as receptor binding of VEGF, signal transduction of VEGF, migration of proliferating endothelial cells, and tube formation. However, it is uncertain that the inhibition of angiogenic cascade is able to lead tumor regression. ANET is different from the traditional anti-angiogenic therapy, since this therapy eradicates proliferating endothelial cells and is expected to eradicate tumor cells through complete cutoff the blood supply to tumor tissues resulting in regression of the tumors. Moreover, ANET would not be expected to acquire drug-resistance, and would inhibit hematogenous metastases.

In here, we showed the therapeutic efficacies of ANET in orthotopic pancreatic tumor model by using tumor neovasculature-targeted liposome encapsulating an anti-cancer drug, ADM. Since pancreatic cancer is known as hypovascular cancer, injury of the small number of vascular cells may affect on large extent of cells that depend on supply of oxygen and nutrients to the vessel. Many experiments have been done to treat pancreatic tumor by anti-angiogenic therapy. These results, however, suggest that the effect of anti-angiogenic therapy alone is thought to be inadequate, concomitant treatments with anti-cancer drug or radiation have been tried [16,17]. On the other hand, ANET injures the proliferative angiogenic endothelial cells directly, and is expected to cause complete regression of tumor cells.

At first, we confirmed the model used here had characteristics of hypovascular tumor. As shown in Fig. 1, the CD31 positive area of orthotopic tumor model is significantly smaller

than that of s.c. implanted tumor. The efficiency of ANET in previous study was the case of s.c. implantation model [14]. The present study is for the first time to investigate whether ANET works in hypovascular tumor model. Biodistribution study by using ^{3}H-labeled PEG-Lip and APRPG-PEG-Lip showed no differences in the accumulation of liposome in the tumor. In general, PEG-modification prevents liposomes from opsonization and reticuloendothelial system (RES)-trapping [18]. This enables liposomes to circulate a long time in bloodstream and to accumulate in the interstitial spaces of tumor tissue through leaking out of angiogenic vessels: This behavior is due to so-called EPR effect [19,20], and such accumulation is called as passive targeting. APRPG peptide-modification adds an ability to actively interact with the angiogenic vessels, although the total accumulation of PEG-Lip and APRPG-PEG-Lip in the tumor was not significantly different. This result is consistent with our previous study using s.c. implanted tumor. We previously observed that the accumulation of PEG-Lip and APRPG-PEG-Lip was quite similar in s.c. implanted tumor model [14], but the intratumoral distribution was much different: PEG-Lip accumulated around angiogenic vessels, and APRPG-PEG-Lip associated with angiogenic vessels [15]. Therefore, we next determined the intratumoral distribution of the two liposomes by using confocal laser scan microscopy. On the other hand, biodistribution study showed the spleen and liver retention of liposomes. This retention is much lower than that of liposome without PEG-modification and the drug in them would show little effect on non-proliferative cells.

As shown in Fig. 3, APRPG-PEG-Lip and PEG-Lip were mainly distributed inside of vessel like structure after 2 h injection. Since these liposomes had long-circulating characteristics, they would effectively reach the vessel of the pancreatic tumor. Intravessel distribution of liposomes, however, was much different in these two kinds of liposomes. APRPG-PEG-Lip was colocalized with vessel marker CD31, although PEG-Lip was rather evenly distributed inside the vessel like structure. The accumulation of PEG-Lip at outside of vessels was not observed at this time point, although these vessels should be angiogenic vessels since APRPG-PEG-Lip having affinity to only neovessels associated with the vessels. The target of APRPG peptide is unclear at present, however, cellular uptake of APRPG-modified liposome significantly increased in VEGF-stimulated human umbilical vein endothelial cells (HUVECs) *in vitro* suggesting that some molecule which was expressed on the surface of the cells by the stimulation is responsible for the interaction. Moreover, a previous paper reported that one peptide including the PRP motif had an affinity for VEGF receptor [21]. Therefore, APRPG peptide may interact with endothelial cells through a certain molecule on the cell surface.

Finally, we examined the effect of ANET on the pancreatic tumor, and observed significant suppression of tumor growth by the treatment with APRPG-PEG-Lip encapsulating ADM. Since APRPG-PEG-Lip directly associated with growing angiogenic endothelial cells, ADM in the liposome might damage the angiogenic vessels. Generally, in pancreatic cancer, scirrhous gastric cancer and inflammatory breast cancer, drug carrier-based DDS require a long-distance transportation to get to the tumor cells which is a disadvantage for targeting DDS. PEG-Lip accumulated passively is thought to remain in large volume of stroma exists in pancreatic cancer, followed by poor anti-tumor activity. The APRPG-based anti-neovascular system may overcome this disadvantage by directly and effectively injuring targeted proliferative angiogenic vessels. Immunohistochemical analysis also supported the idea.

In conclusion, ANET has the possibility to treat hypovascular pancreatic tumor by injuring the neovessels. APRPG-modification of PEG-Lip endows it with binding ability to angiogenic endothelial cells, therefore ADM encapsulated in the liposome may effectively damage the cells, which causes enhanced therapeutic efficacy compared to that by ADM in PEG-Lip. Since PEG-Lip accumulated in orthotopic pancreatic tumor in a similar extent to APRPG-PEG-Lip, the inferior therapeutic efficacy of ADM in PEG-Lip to that in APRPG-PEG-Lip might be due to the topological distribution difference: PEG-Lip might reside in the interstitial spaces of the tumor, and gradually release ADM which causes damage of growing cells.

References

[1] A. Jemal, T. Murray, A. Samuels, A. Ghafoor, E. Ward, M.J. Thun, Cancer statistics, CA Cancer J. Clin. 53 (1) (2003) 5–26.
[2] D.R. Martin, R.C. Semelka, MR imaging of pancreatic masses, Magn. Reson. Imaging Clin. N. Am. 8 (4) (2000) 787–812.
[3] J. Rosai, in: J. Rosai (Ed.), Ackerman's Surgical Pathology, 8th ed, Mosby, St. Louis, 1996, pp. 969–1013.
[4] R.C. Semelka, L.L. Nagase, D. Armao, et al., in: R.C. Semelka (Ed.), Abdominal-Pelvic MRI, 2nd ed, Wiley–Liss, New York, 2002, pp. 373–490.
[5] C.J. Bruns, C.C. Solorzano, M.T. Harbison, S. Ozawa, R. Tsan, D. Fan, J. Abbruzzese, P. Traxler, E. Buchdunger, R. Radinsky, I.J. Fidler, Blockade of the epidermal growth factor receptor signaling by a novel tyrosine kinase inhibitor leads to apoptosis of endothelial cells and therapy of human pancreatic carcinoma, Cancer Res. 60 (11) (2000) 2926–2935.
[6] R.G. Chirivi, A. Garofalo, M.J. Crimmin, L.J. Bawden, A. Stoppacciaro, P.D. Brown, R. Giavazzi, Inhibition of the metastatic spread and growth of B16-BL6 murine melanoma by a synthetic matrix metalloproteinase inhibitor, Int. J. Cancer 58 (3) (1994) 460–464.
[7] S.A. Eccles, G.M. Box, W.J. Court, E.A. Bone, W. Thomas, P.D. Brown, Control of lymphatic and hematogenous metastasis of a rat mammary carcinoma by the matrix metalloproteinase inhibitor batimastat (BB-94), Cancer Res. 56 (12) (1996) 2815–2822.
[8] H. Hurwitz, L. Fehrenbacher, W. Novotny, T. Cartwright, J. Hainsworth, W. Heim, J. Berlin, A. Baron, S. Griffing, E. Holmgren, N. Ferrara, G. Fyfe, B. Rogers, R. Ross, F. Kabbinavar, Bevacizumab plus irinotecan, fluorouracil, and leucovorin for metastatic colorectal cancer, N. Engl. J. Med. 350 (23) (2004) 2335–2342.
[9] B.A. Teicher, N.P. Dupuis, M.F. Robinson, Y. Emi, D.A. Goff, Antiangiogenic treatment (TNP-470/minocycline) increases tissue levels of anticancer drugs in mice bearing Lewis lung carcinoma, Oncol. Res. 7 (5) (1995) 237–243.
[10] H. Satoh, H. Ishikawa, M. Fujimoto, M. Fujiwara, Y.T. Yamashita, T. Yazawa, M. Ohtsuka, S. Hasegawa, H. Kamma, Angiocytotoxic therapy in human non-small cell lung cancer cell lines-advantage of combined effects of TNP-470 and SN-38, Acta Oncol. 37 (1) (1998) 85–90.
[11] N. Oku, T. Asai, K. Watanabe, K. Kuromi, M. Nagatsuka, K. Kurohane, H. Kikkawa, K. Ogino, M. Tanaka, D. Ishikawa, H. Tsukada, M. Momose, J. Nakayama, T. Taki, Anti-neovascular therapy using novel peptides homing to angiogenic vessels, Oncogene 21 (17) (2002) 2662–2669.
[12] T. Asai, M. Nagatsuka, K. Kuromi, S. Yamakawa, K. Kurohane, K. Ogino, M. Tanaka, T. Taki, N. Oku, Suppression of tumor growth by novel peptides homing to tumor-derived new blood vessels, FEBS Lett. 510 (3) (2002) 206–210.

[13] N. Maeda, Y. Takeuchi, M. Takada, Y. Namba, N. Oku, Synthesis of angiogenesis-targeted peptide and hydrophobized polyethylene glycol conjugate, Bioorg. Med. Chem. Lett. 14 (4) (2004) 1015–1017.
[14] N. Maeda, Y. Takeuchi, M. Takada, Y. Sadzuka, Y. Namba, N. Oku, Anti-neovascular therapy by use of tumor neovasculature-targeted long-circulating liposome, J. Control. Release 100 (1) (2004) 41–52.
[15] N. Maeda, S. Miyazawa, K. Shimizu, T. Asai, S. Yonezawa, S. Kitazawa, Y. Namba, H. Tsukada, N. Oku, Enhancement of anticancer activity in antineovascular therapy is based on the intratumoral distribution of the active targeting carrier for anticancer drugs, Biol. Pharm. Bull. 29 (9) (2006) 1936–1940.
[16] C.H. Crane, L.M. Ellis, J.L. Abbruzzese, C. Amos, H.Q. Xiong, L. Ho, D.B. Evans, E.P. Tamm, C. Ng, P.W. Pisters, C. Charnsangavej, M.E. Delclos, M. O'Reilly, J.E. Lee, R.A. Wolff, Phase I trial evaluating the safety of bevacizumab with concurrent radiotherapy and capecitabine in locally advanced pancreatic cancer, J. Clin. Oncol. 24 (7) (2006) 1145–1151.
[17] H.L. Kindler, G. Friberg, D.A. Singh, G. Locker, S. Nattam, M. Kozloff, D.A. Taber, T. Karrison, A. Dachman, W.M. Stadler, E.E. Vokes, Phase II trial of bevacizumab plus gemcitabine in patients with advanced pancreatic cancer, J. Clin. Oncol. 23 (31) (2005) 8033–8040.
[18] N. Oku, Anticancer therapy using glucuronate modified long-circulating liposomes, Adv. Drug Deliv. Rev. 40 (1–2) (1999) 63–73.
[19] D.T. Auguste, R.K. Prud'homme, P.L. Ahl, P. Meers, J. Kohn, Association of hydrophobically-modified poly(ethylene glycol) with fusogenic liposomes, Biochim. Biophys. Acta 1616 (2) (2003) 184–195.
[20] H. Maeda, J. Wu, T. Sawa, Y. Matsumura, K. Hori, Tumor vascular permeability and the EPR effect in macromolecular therapeutics: a review, J. Control. Release 65 (1–2) (2000) 271–284.
[21] R.J. Giordano, M. Cardo-Vila, J. Lahdenranta, R. Pasqualini, W. Arap, Biopanning and rapid analysis of selective interactive ligands, Nat. Med. 7 (11) (2001) 1249–1253.